Electronic Supplementary Information

Systematic Study of Zeolitic Imidazolate Frameworks for Enhanced Electrochemical Aldehyde Sensing

Martyna Mańka,[a, b] Wojciech Kukułka,[c] Mateusz Wlazło,[d] Violetta Patroniak,*[b] Artur Ciesielski,[a, c] Verónica Montes-García,*[a] Paolo Samorì*[a]

[a] Université de Strasbourg, CNRS, ISIS 8 allée Gaspard Monge, Strasbourg 67000, France. E-mail: samori@unistra.fr, montesgarcia@unistra.fr

[b] Faculty of Chemistry, Adam Mickiewicz University, Uniwersytetu Poznańskiego 8, Poznań 61-614, Poland.

[c] Centre for Advanced Technologies, Adam Mickiewicz University, Uniwersytetu Poznańskiego 10, Poznań 61-614, Poland.

[d] Chemical and Biological Systems Simulation Lab, Centre of New Technologies, University of Warsaw, 02-097 Warsaw, Poland.

Table of Contents

Section A. Materials and characterization

Materials

2-methylimidazole, 2-aminobenzimidazole, zinc nitrate hexahydrate, cobalt nitrate hexahydrate, acetaldehyde, benzaldehyde, formaldehyde, ACS reagent, 37 wt. % in H_2O, contains 10-15% methanol as stabilizer (to prevent polymerization), potassium hexacyanoferrate(III) were purchased from Sigma Aldrich. Nafion was supplied by tebubio. Methanol was supplied by CARLO ERBA Reagents, ethanol was supplied by Fisher, MicroPolish powders were purchased from CH Instruments. All the materials were used without further purification.

Methods

Powder X-ray diffraction (PXRD): Structural data were obtained by PXRD with the use of Bruker AXS D8 Advance diffractometer (2θ resolution: ±0.01°) in Bragg-Brentano geometry with CuKα1 radiation (λ = 1.5406 Å).

Fourier-transform infrared (FT-IR) spectroscopy: The FT-IR spectra were recorded in a range between 4000 and 400 cm^{-1} using Bruker FT-IR IFS 66/s spectrometer.

X-ray photoelectron spectroscopy (XPS): XPS analyses were performed with a Thermo Scientific Kα X-ray Photoelectron Spectrometer system equipped with an Al Kα X-Ray source.

Scanning electron microscopy (SEM): SEM images were obtained with a FEI Quanta 250 FEG Scanning Electron Microscope, operating in a high vacuum mode with accelerating voltages of 30 kV for the incident beam, after coating the sample with gold using a sputter coater (ambient temperature, pressure in 10^{-4} mbar range in a N_2 atmosphere, sputtered for 40 s from a solid gold target at a current of 60 mA).

Brunauer, Emmett and Teller (BET) model and Horvath-Kawazoe (H-K) method for micropore size analysis were used with an nitrogen adsorption-desorption isotherms measurements with ASAP 2420 (Micromeritics).

Thermogravimetric analysis (TGA) was performed using the TGA/DSC1 (Mettler Toledo) instrument at the heating rate of 10 °C/min from room temperature to 1000 °C in nitrogen to study the thermal stability and mass loss of the samples.

Density functional theory (DFT) calculations were performed using the planewave spin-polarized DFT at the PBE/D3(BJ) level of theory with Vienna Ab Initio Simulation Package (VASP). Prepared structures were relaxed in terms of lattice and atomic degrees of freedom until forces were below 0.03 eV/Å.

Synthesis

Synthesis of ZIF-8: ZIF-8 was synthesized using a reported protocol.[1, 2] Briefly, 950 mg (11.57 mmol) of 2-methylimidazole was dissolved in 15 mL of methanol and then added to a solution of 361.5 mg (12.15 mmol) of zinc nitrate hexahydrate in 10 mL methanol. The solution containing the organic linker was added to the salt solution. The resulting mixture was stirred for 24 hours at room temperature. The obtained white precipitate was separated by centrifugation at RCF 4430 g (6000 rpm) for 20 minutes and washed with methanol 3 times. The obtained powder was air-dried at room temperature and then activated under vacuum for 16 hours at 120 ^{o}C.[1]

Synthesis of ZIF-67: ZIF-67 was synthesized according to a modified reported protocol.[1] Briefly, 950 mg (11.57 mmol) of 2-methylimidazol was dissolved in 15 mL methanol and then added to the solution of 361.5 mg (12.42 mmol) of cobalt nitrate hexahydrate in 10 mL methanol. The mixture was stirred for 24 hours at room temperature. The obtained product was separated by centrifugation at RCF 4430 g (6000 rpm) for 20 minutes and washed with methanol 3 times. The obtained powder was air-dried at room temperature and activated under vacuum for 16 hours at 120^{o} C.[1]

Synthesis of NH_2-ZIF-7: NH_2-ZIF-7 was synthesized using a modified reported protocol.[1] Briefly, a solution of 950 mg (7.13 mmol) of 2-aminobenzimidazole in 15 mL of methanol was added to a solution of 361.5 mg (12.15 mmol) of zinc nitrate hexahydrate in 10 mL of methanol. The mixture was stirred for 24 hours at room temperature. The obtained clear solution was evaporated and the precipitate was washed with methanol 3 times and separated by centrifugation at RCF 4430 g (6000 rpm) for 20 minutes. The obtained powder was air-dried at room temperature and then activated under vacuum for 16 hours at 120 ^{o}C.[1]

Synthesis of NH_2-ZIF-9: NH_2-ZIF-9 was synthesized using a modified reported protocol.[1] Briefly, 361 mg (7.13 mmol) of cobalt nitrate hexahydrate was dissolved in 10 mL of methanol and then added to a solution of 950 mg (12.42 mmol) of 2-aminobenzimidazole dissolved in 10 mL of methanol. Then, the obtained mixture was stirred for 24 hours at room temperature. The obtained clear solution was evaporated and the precipitate was washed with methanol 3 times and separated by centrifugation

at RCF 4430 g (6000 rpm) for 20 minutes. The obtained powder was air-dried at room temperature and then activated under vacuum for 16 hours at 120°C.[1]

Chemical stability study of ZIFs: A certain amount of aldehydes (59.5 µL of acetaldehyde, 44.8 µL of benzaldehyde or 57.16 µL of formaldehyde) was added to a dispersion of ZIF in a mixture of ethanol:water. The amounts of ethanol and water depend on the specific aldehydes, being 454.1 µL and 1.876 mL, respectively, for acetaldehyde, 457 µL and 1.828 mL, respectively, for benzaldehyde and 454.5 µL and 1.818 mL for formaldehyde. The solution was stirred for 24 hours at room temperature and then centrifuged at RCF 4430 g (6000 rpm). The obtained powder was air-dried at room temperature.[3]

Preparation of ZIF-modified glassy carbon electrode (ZIF@GCE): The obtained ZIF powder (10 mg) was dispersed in a mixture of ethanol (350 µl) and water (150 µl). Then, 5 µL of Nafion was added and the suspension was sonicated in water ultrasonic bath for one hour. Prior to the ZIF deposition, the GCE (diameter of 4 mm) was polished and washed with MiliQ water. 20 µL of dispersed material (20 mg/mL) was drop casted onto the electrode and air-dried at room temperature to obtain ZIF@GCE.

Electrochemical characterization: Electrochemical impedance spectroscopy (EIS) was performed in a three-electrode system (ZIF@GCE as a working electrode, Ag/AgCl reference electrode and platinum wire as a counter electrode) with an Autolab PGSTAT204 Potentiostat/Galvanostat instrument. The impedance spectra were collected in the frequency range of 0.1 – $5 \cdot 10^5$ Hz, swept from high to low frequencies, with a sine-wave voltage signal amplitude of 10 mV (root-mean-square, RMS). The device impedance (Z) was converted into capacitance (Cp) using a simple parallel resistor-capacitor (RC) circuit (SI). The following equation was employed:

$$C_p = \frac{-Z''}{\omega |Z|^2} \qquad \text{(equation S1)}$$

Where Z" represents the imaginary part of the impedance and ω is the angular frequency.[4]

Electrochemical sensing of aldehydes in MilliQ water: Potassium hexacyanoferrate(III) (0.5 $mmol \cdot L^{-1}$) was used as an electrolyte. The electrochemical performance of all the ZIFs was assessed for the detection of acetaldehyde, benzaldehyde and formaldehyde. EIS measurements were performed after 5 minutes of immersing the electrodes in the solution containing the electrolyte and the specific aldehyde concentrations (0-1 mM).

Logarithmic fittings were performed for each aldehyde by plotting the Cp versus the logarithm of aldehyde concentration. Sensitivity was obtained from the slope of the logarithmic fittings. Limit of detection (LOD) of the different ZIF@GCE were calculated using following equation:

$$LOD = \frac{(3\ SD)}{\sigma} \qquad \text{(equation S2)}$$

Where SD is the standard error of the regression and σ is the sensitivity.[2]

Detection of aldehydes in real-world samples: Tap water was filtered using polytetrafluoroethylene (PTFE) hydrophilic membrane (pore size: 45 µm). Subsequently, aldehydes were added to achieve concentrations of 10, 30 or 50 µM. EIS measurements were performed after 5 minutes of immersing the electrodes in the solution containing the electrolyte and the specific aldehyde concentrations. The aldehyde concentrations were calculated by using the logarithmic fittings obtained for the different aldehydes in MilliQ water.

Section B. Physical characterization

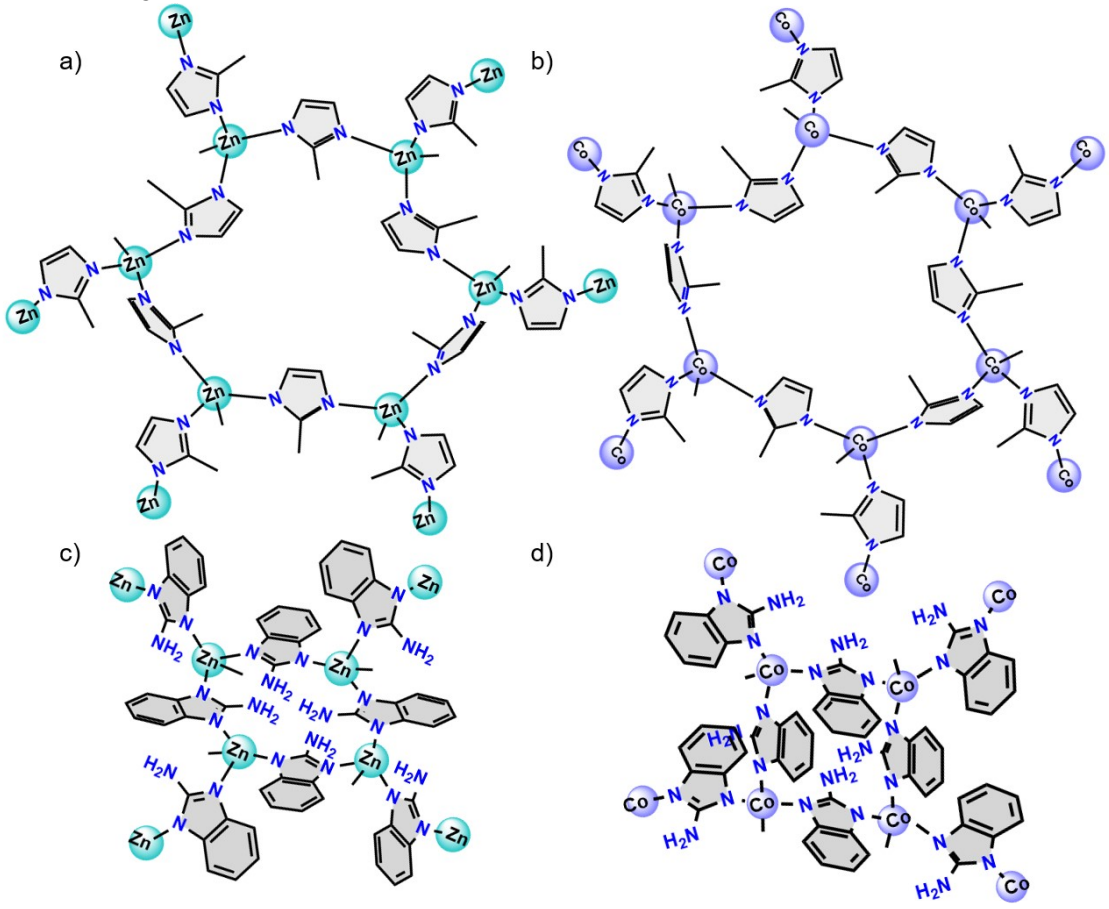

Fig. S1. Schematic structures of a) ZIF-8, b) ZIF-67, c) NH_2-ZIF-7 and d) NH_2-ZIF-9.

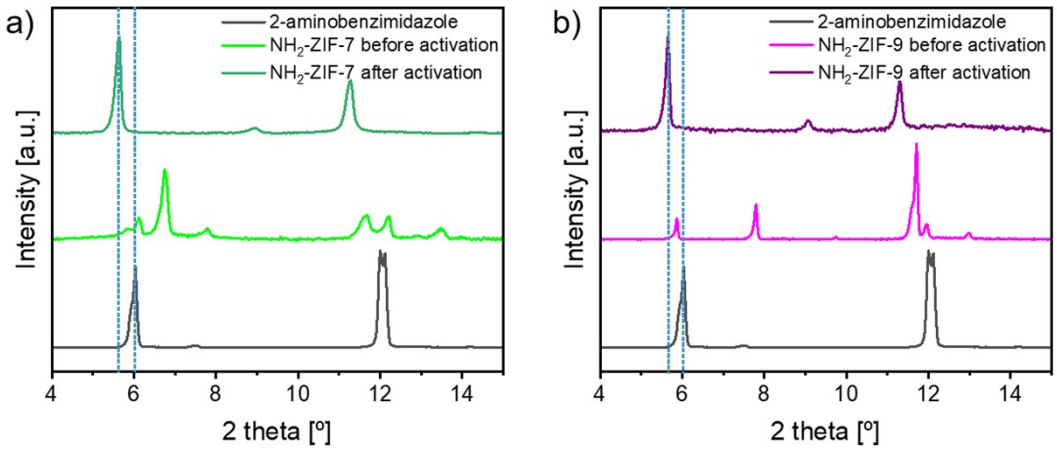

Figure S2. Magnification of the PXRD spectra before and after thermal activation of a) ZIF-8, and b) NH_2-ZIF-7. The PXRD spectrum of the corresponding organic linker is included for comparison for each ZIF.

On the XRD of the 2-aminobenzidimazole monomer, reflections can be seen at 6.36°, 7.52°, 12.00°, 14.25°, 17.01°, 18.14°, 19.33°, 20.40°, 22.38°, 2.65°, 22.89°, 24.34°, 25.50°, 27.04°, 27.64°, 28.05°, 29.24°, 30.22°, 30.58°, 49.98°. Differently, after activation at 120 °C, there are peaks at 5.65°, 8.94° and 11.32° in case of NH_2-ZIF-7 and at 5.65°, 8.94° and 11.32° in case of NH_2-ZIF-9. Special attention should be paid to the area from 4.46° to 13.90°, where it can be noticed that, in particular, the second reflection is located in a completely different place on the XRD of the ZIF than that of the monomer.

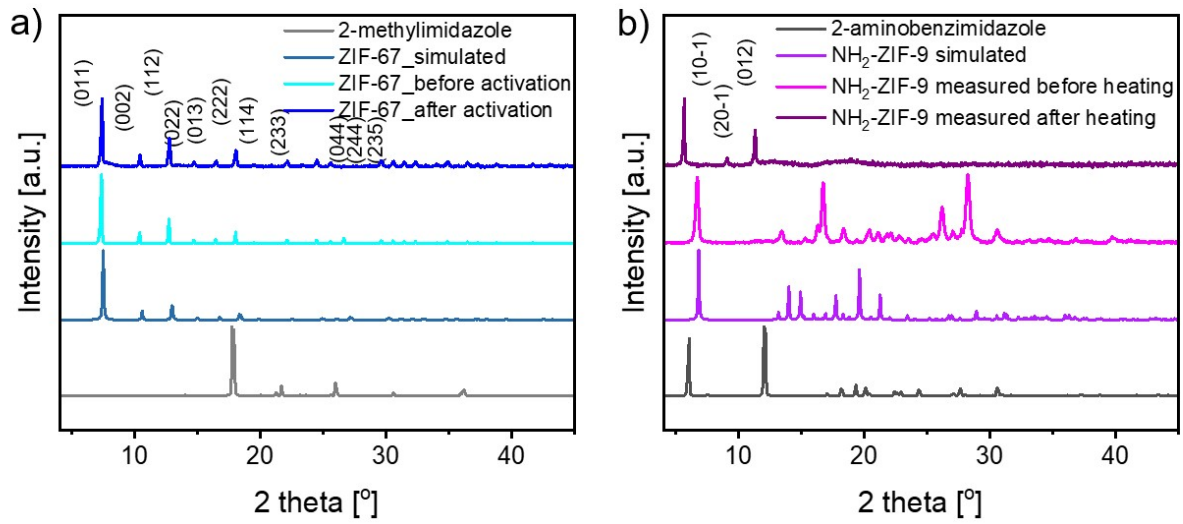

Figure S3. Normalized PXRD spectra before and after thermal activation of a) ZIF-67 and b) NH_2-ZIF-9. The simulated PXRD spectra of the ZIFs and the PXRD spectrum of the corresponding organic linker are included for comparison for each ZIF.

Interestingly, the PXRD spectra of NH_2-ZIF-7 and NH_2-ZIF-9 are altered upon thermal activation, with several reflexes disappearing. ZIFs are known for their unique flexibility, which allows them to undergo phase changes due to external factors such as temperature, pressure, or exposure to solvents. When ZIFs are heated to 120 °C, any guest molecules within the ZIF structure, such as methanol or water residues from the synthesis process, are removed. This removal reduces steric crowding within the framework, enabling the imidazole linkers to rotate and adopt configurations associated with a narrower pore phase.[5] Furthermore, the heating process can distort the metal tetrahedral environment, leading to variations in the N-metal-N bond angles. These structural changes contribute to a phase transition and are often accompanied by a reduction in symmetry within the crystal structure.[6] Such transformations are intrinsic to the dynamic nature of ZIFs and are well-documented in the literature.

ZIF-8 exhibits the first intense peak at a low angle of 7.28° (2θ), which corresponds to the (011) reflection plane, along with minor peaks at 10.31º; 12.62º; 14.64º; 16.39º; 17.99º; 22.18º; 24.43º; 26.60º; 29.57º; 31.46º and 32.30º attributed to the 002; 112; 022; 013; 222; 114; 233; 134; 044; 244 and 235 reflection planes, respectively.[7]

ZIF-67 exhibits the first intense peak at a low angle of 7.37° (2θ), which corresponds to the (011) reflection plane, along with minor peaks at 10.43º; 12.74º; 14.73º; 16.48º; 18.05º; 22.12º;

24.44º; 25.59º; 26.64º; 29.57º; 31.44º and 32.36º attributed to the 002; 112; 022; 013; 222; 114; 233; 044; 244 and 235 reflection planes, respectively.[8]

In both cases, peaks (011), (002), (112), (022), (013) and (222) are indexed to the unit cell of SOD-type ZIF-8/ZIF-67 and confirm its high crystallinity. Peaks (002), (022) and (013) can be attributed to the pseudopolymorfism of ZIF caused by a partial deprotonation of 2-methylimidazole.[9]

NH_2-ZIF-7 exhibits the first intense peaks at a low angle of 6.10°; 6.78° and 7.79° (2θ), which corresponds to (10-1), (110) and (1-1-1) reflection planes, respectively, along with the minor peaks at 11.67° 12.21°; 13.48°; 15.38°; 16.30°; 16.75°; 18.23°; 19.42°; 20.16°; 21.11°; 22.53°; 26.21°; 27.70º; 28.26º and 30.52° attributed to the (102); (012); (02-2); (3-30); (4-20); (2-32); (410); (4-12); (5-10); (303); (042); (6-11); (4-24); (4-34) and (-25-4) reflection planes, respectively. After activation at 120 °C degrees, most of the peaks disappeared, confirming the phase change in which the compound occurs. After activation, reflections remained at 5.65°, 8.94° and 11.32° attributed to the (10-1), (20-1) and (012) reflection planes, respectively.

NH_2-ZIF-9 exhibits the first intense peak at a low angle of 6.66° (2θ), which corresponds to (002) reflection plane, along with the minor peaks at 13.34°; 15.18°; 16.70°; 18.29°; 19.42°; 20.31°; 21.14°; 21.85°; 23.48°; 24.61°; 25.32°; 26.24°; 27.04°; 28.29°; 30.58° attributed to the (2-2-1); (22-2); (004); (3-12); (223); (1-33); (2-3-3); (31-4); (2-24); (4-3-1); (150); (006); (03-5); (404); (44-3) reflection planes, respectively. After activation at 120 °C degrees, most of the peaks disappeared, confirming the phase change in which the compound occurs. After activation, reflections remained at 5.65°, 8.94° and 11.32° attributed to the (10-1), (20-1) and (012) reflection planes, respectively.

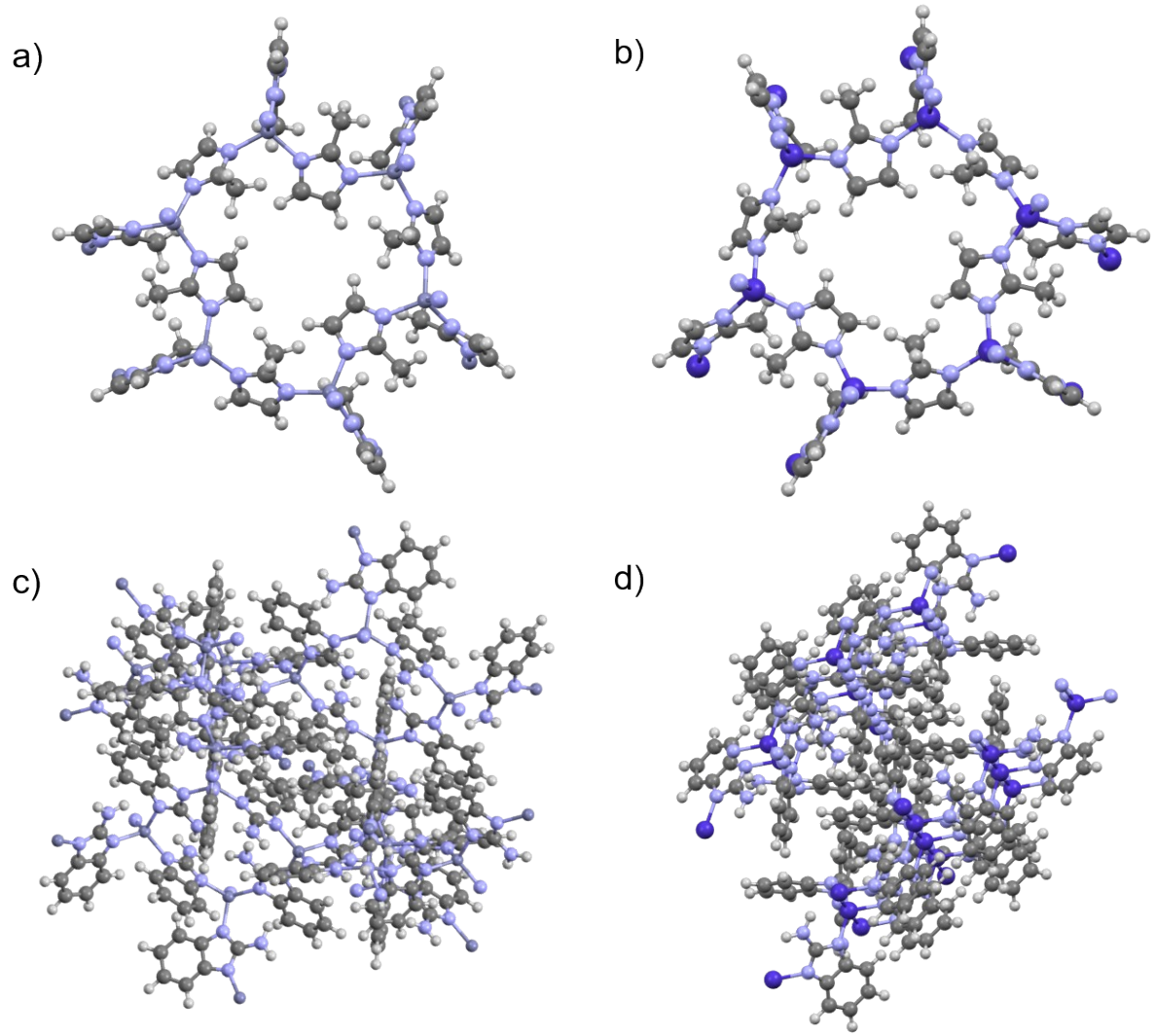

Figure S4. Simulated XRD structures of a) ZIF-8, b) ZIF-67, c) NH_2-ZIF-7 and d) NH_2-ZIF-9.

Tables S1. Cell parameters of the different ZIFs.

ZIF-8	ZIF-67	NH_2-ZIF-7	NH_2-ZIF-9
C48 H60 N24 Zn6	C48 H60 Co6 N24	C252 H180 N72 Zn18	C224 H160 Co16 N64
Space group: P 1	Space group: P 1	Space group: P 1	Space group: P 1
a = 14.16 Å	a = 14.42 Å	a = 21.84 Å	a = 15.89 Å
b = 14.28 Å	b = 14.53 Å	b = 19.97 Å	b = 15.88 Å
c = 14.26 Å	c = 14.51 Å	c = 15.76 Å	c = 18.16 Å
α = 109.8°	α = 109.7°	α = 95.0°	α = 90.0°
β = 109.5°	β = 109.4°	β = 88.8°	β = 97.0°
γ = 109.3°	γ = 109.4°	γ =107.6°	γ = 90.0°
V = 2215.81 Å^3	V = 2336.63 Å^3	V = 6527.78 Å^3	V = 4548.92 Å^3

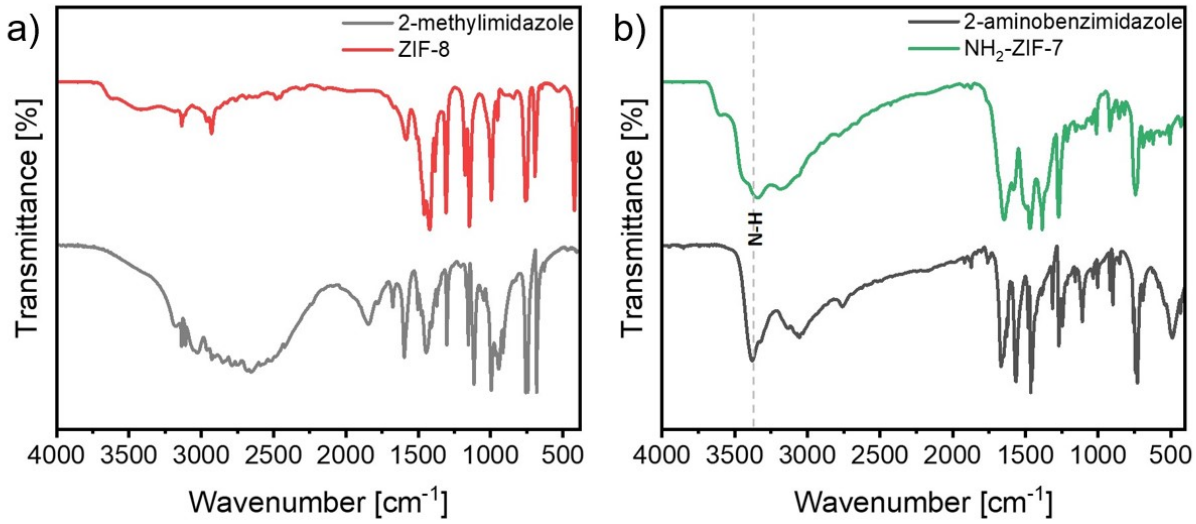

Figure S5. Normalized FT-IR spectra of a) ZIF-8 and b) NH_2-ZIF-7. The FT-IR spectrum of the corresponding organic linker is included for comparison for each ZIF.

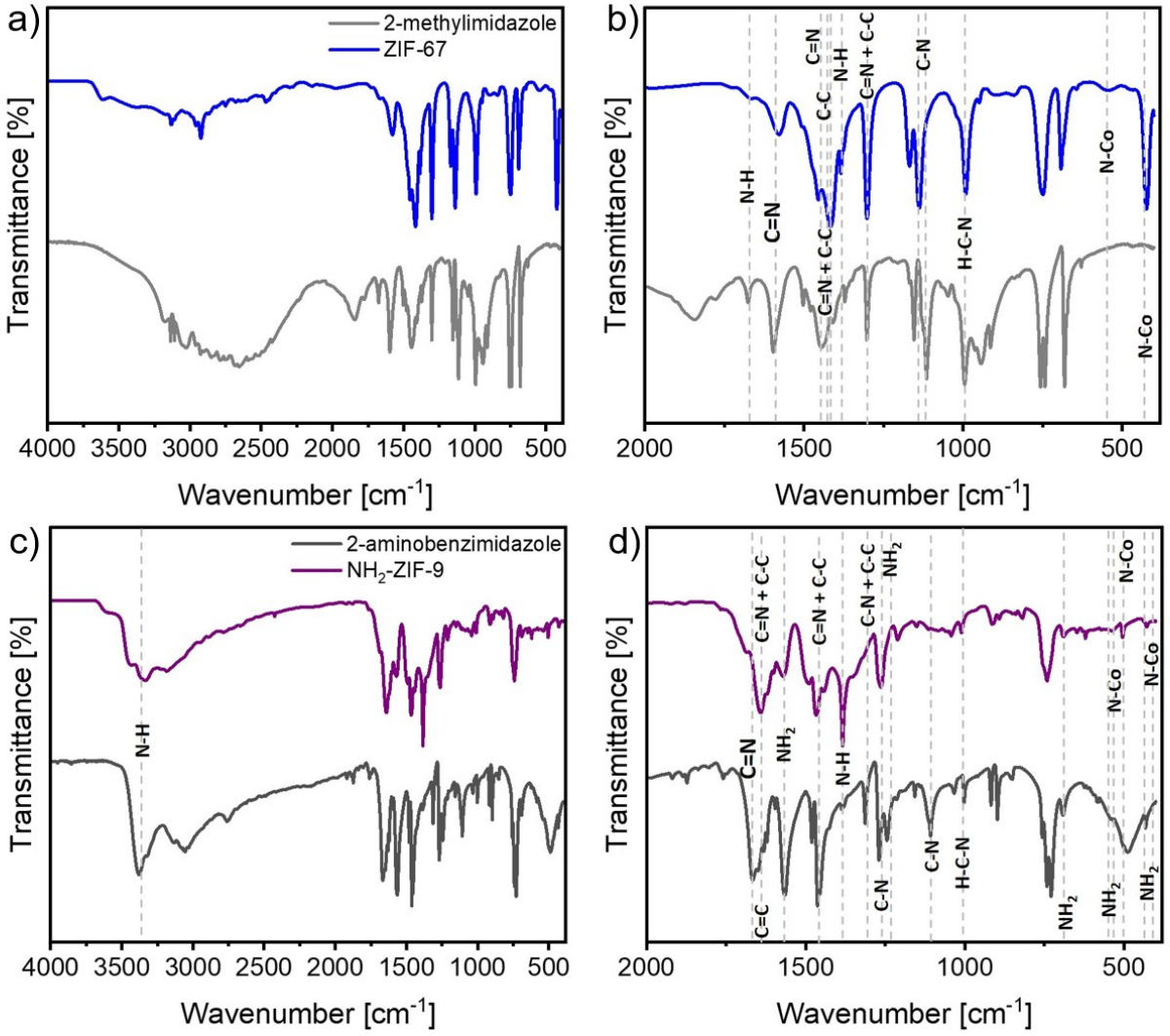

Figure S6. Normalized FT-IR spectra of a-b) ZIF-67 and c-d) NH_2-ZIF-9. The FT-IR spectrum of the corresponding organic linker is included for comparison for each ZIF.

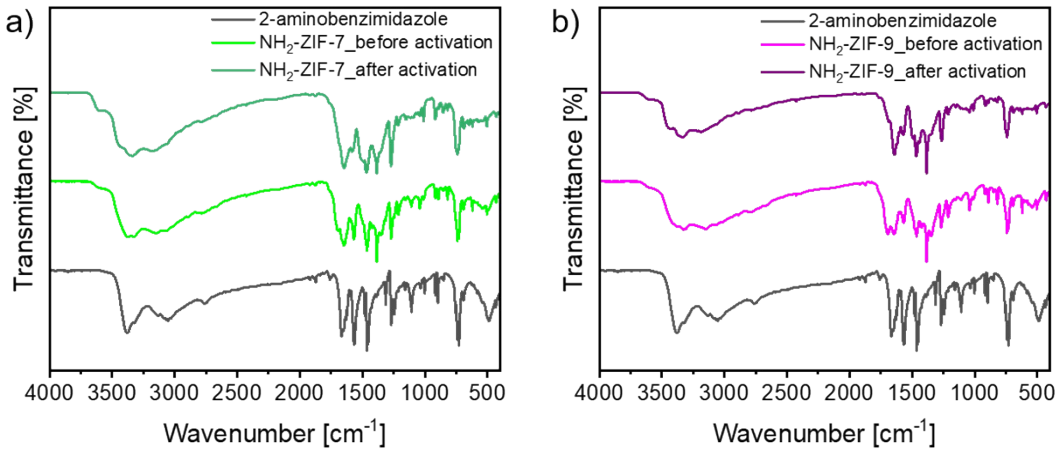

Figure S7. FTIR spectra before and after thermal activation of a) NH_2-ZIF-7, and b) NH_2-ZIF-9. The FTIR spectrum of the corresponding organic linker is included for comparison for each ZIF.

Furthermore, the stability of the ZIF structures following annealing at 120 °C is confirmed by the FT-IR spectra (Figure S7). After activation, the FT-IR spectrum of the ZIFs remains unchanged, providing additional evidence of the chemical stability of the ZIFs upon annealing.

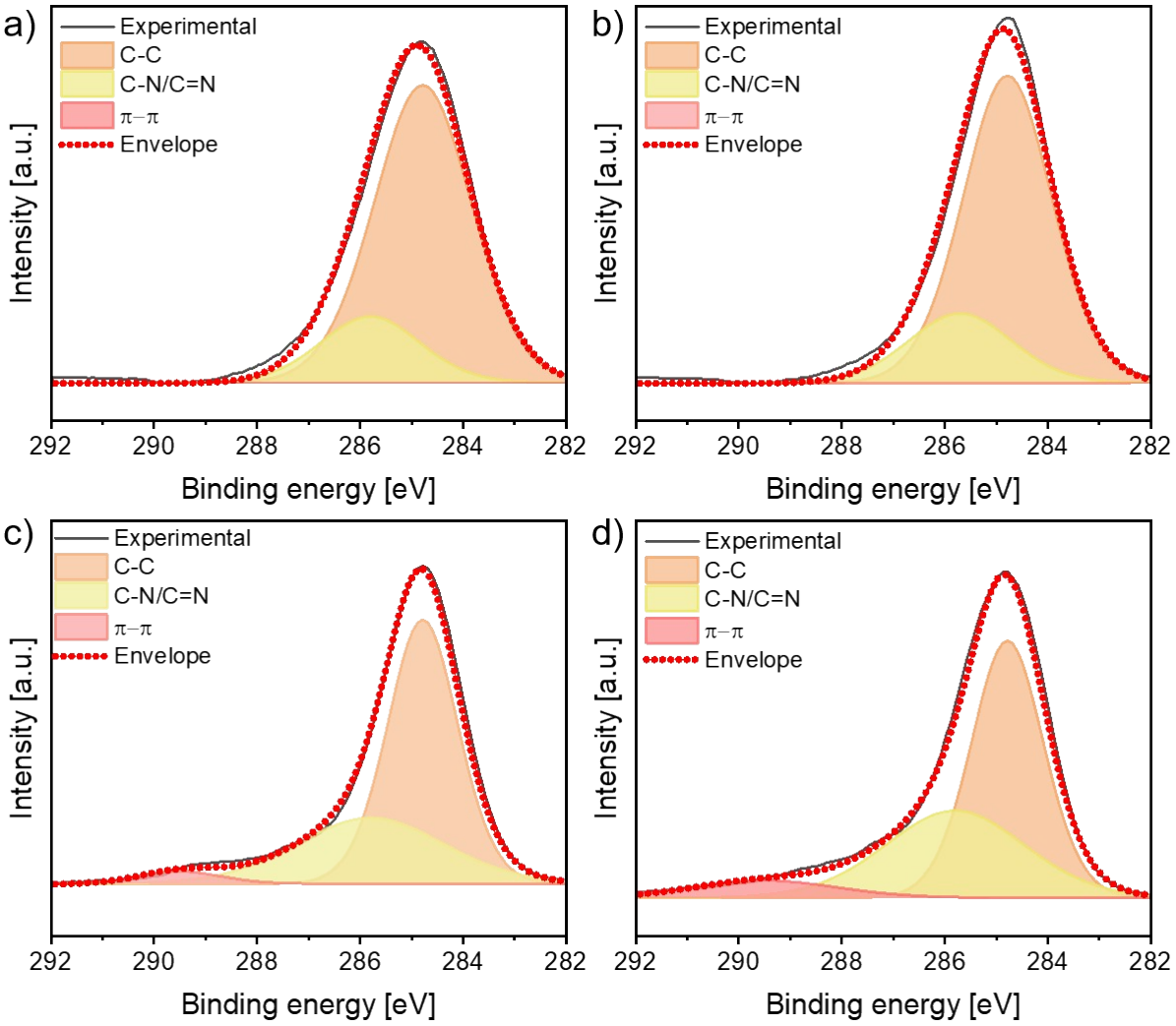

Figure S8. C1s XPS spectra of a) ZIF-8, b) ZIF-67, c) NH_2-ZIF-7, d) NH_2-ZIF-9.

The high-resolution C1s spectra (Fig. S8, ESI†) of all ZIFs display two main peaks centered at 284.78 and 285.80 eV, corresponding to C-C /C=C, and C-N respectively.[10,11] As expected, the contribution of C-N is higher in NH_2-ZIF-7 and NH_2-ZIF-9 compared to ZIF-8 and ZIF-67.

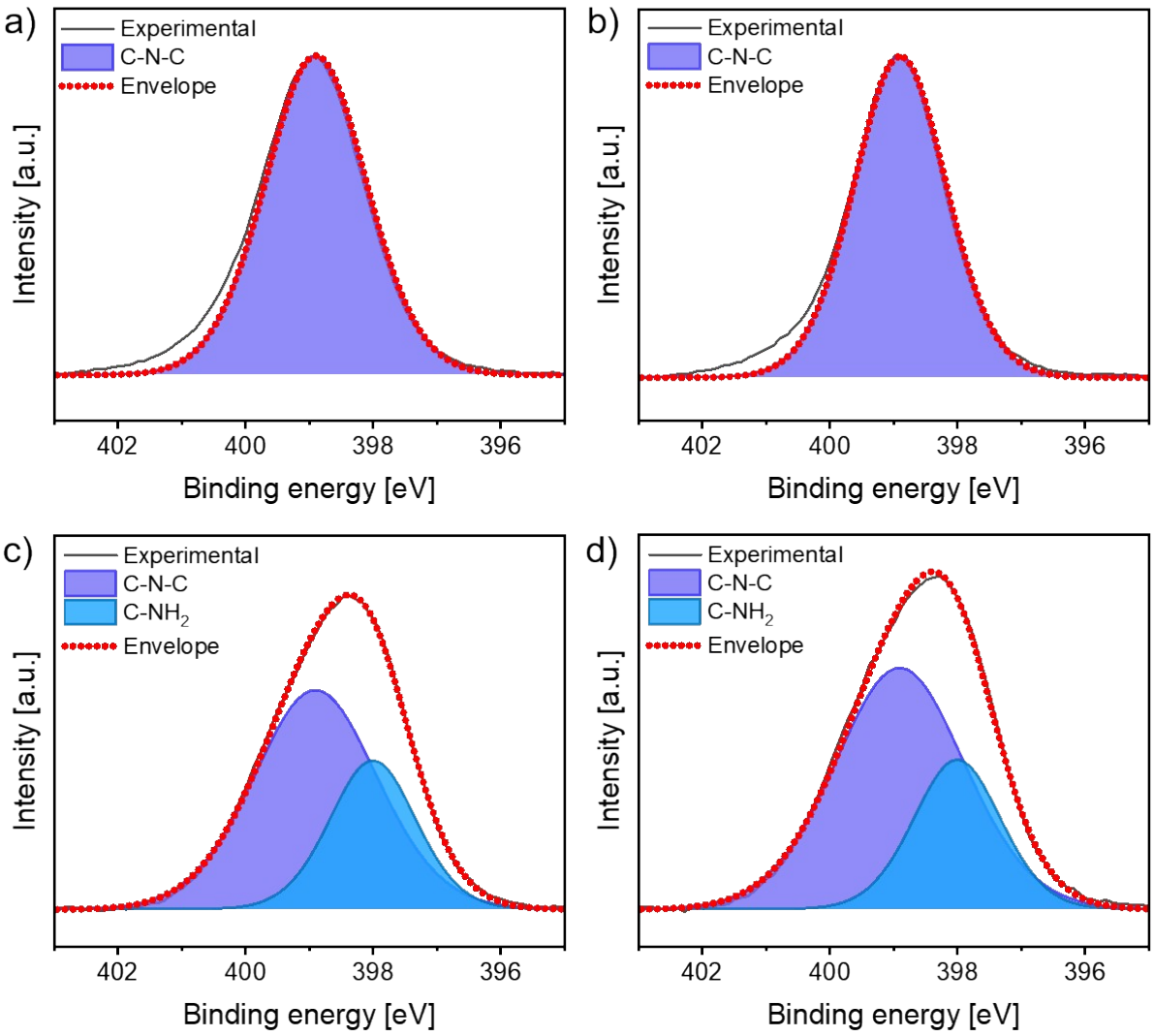

Figure S9. N1s XPS spectra of a) ZIF-8, b) ZIF-67, c) NH_2-ZIF-7, d) NH_2-ZIF-9.

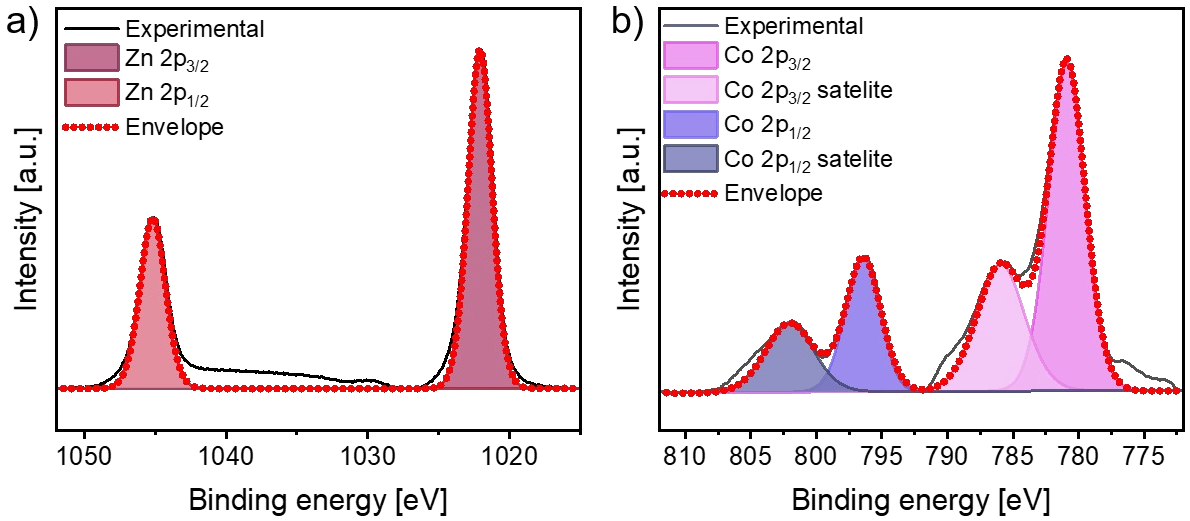

Figure S10. Zn2p XPS spectrum of a) NH_2-ZIF-7. Co2p XPS spectrum of b) NH_2-ZIF-9.

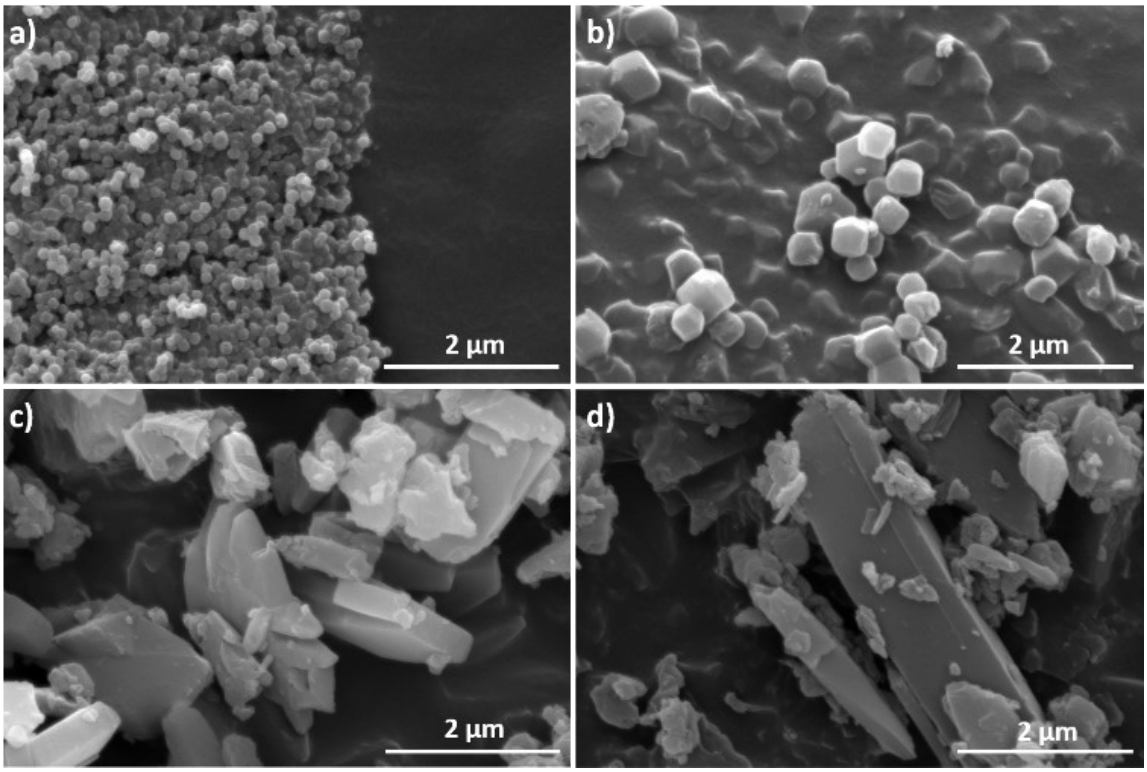

Figure S11. SEM images of a) ZIF-8, b) ZIF-67, c) NH2-ZIF-7 and d) NH2-ZIF-9.

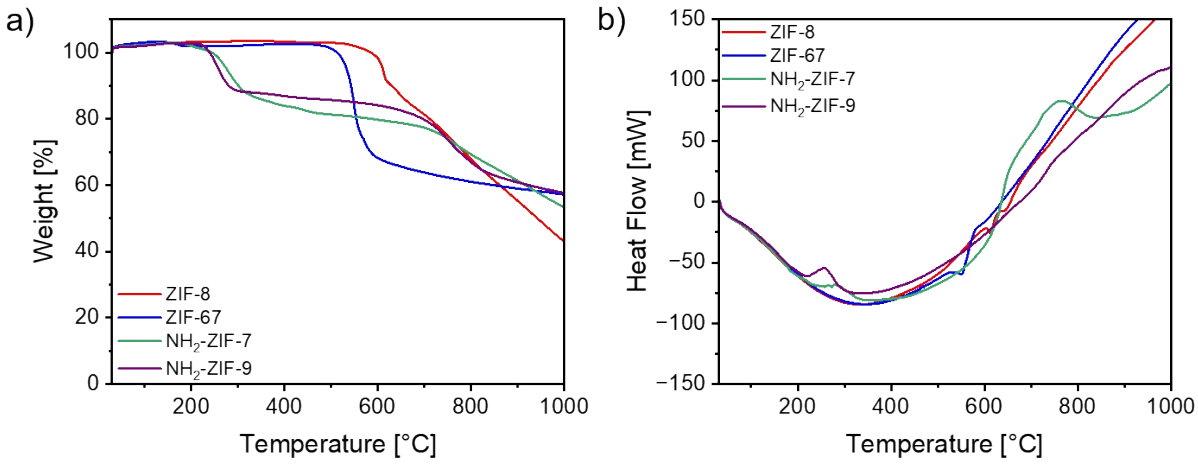

Figure S12. a) TGA and b) DSC of the different ZIFs.

The lower thermal stability of amino-functionalized frameworks could be ascribed to the loss of NH_2 groups.[12]

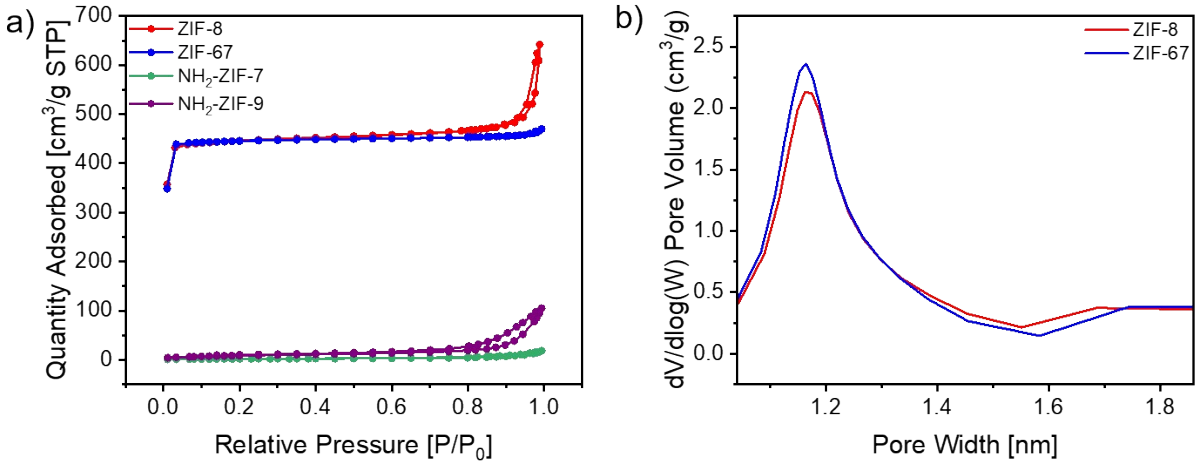

Figure S13. a) BET surface area and b) pore size distribution of the different ZIFs. The pore sizes of NH_2-ZIF-7 and NH_2-ZIF-9 are below the limit of the instrument.

Table S2. Parameters obtained from nitrogen adsorption-desorption analysis.

	Specific Surface Area [m^2/g]	Total Pore Volume [cm^3/g]
ZIF-8	1579.25 ± 17.62	0.84
ZIF-67	1576.01 ± 17.07	0.59
NH_2-ZIF-7	7.48 ± 0.04	0.02
NH_2-ZIF-9	33.37 ± 0.03	0.12

Table S3. The proportion of micropores and remaining pores and average pore width for ZIF-8 and ZIF-67.

	Specific Surface Area [m^2/g]	T-Plot Micropores [m^2/g]	T-Plot External [m^2/g]	Average Pore Width [nm]
ZIF-8	1579.25 ± 17.62	1472.37	106.88	1.2275
ZIF-67	1576.01 ± 17.07	1516.02	59.99	1.2037

Section C. Chemical stability and sensing mechanisms

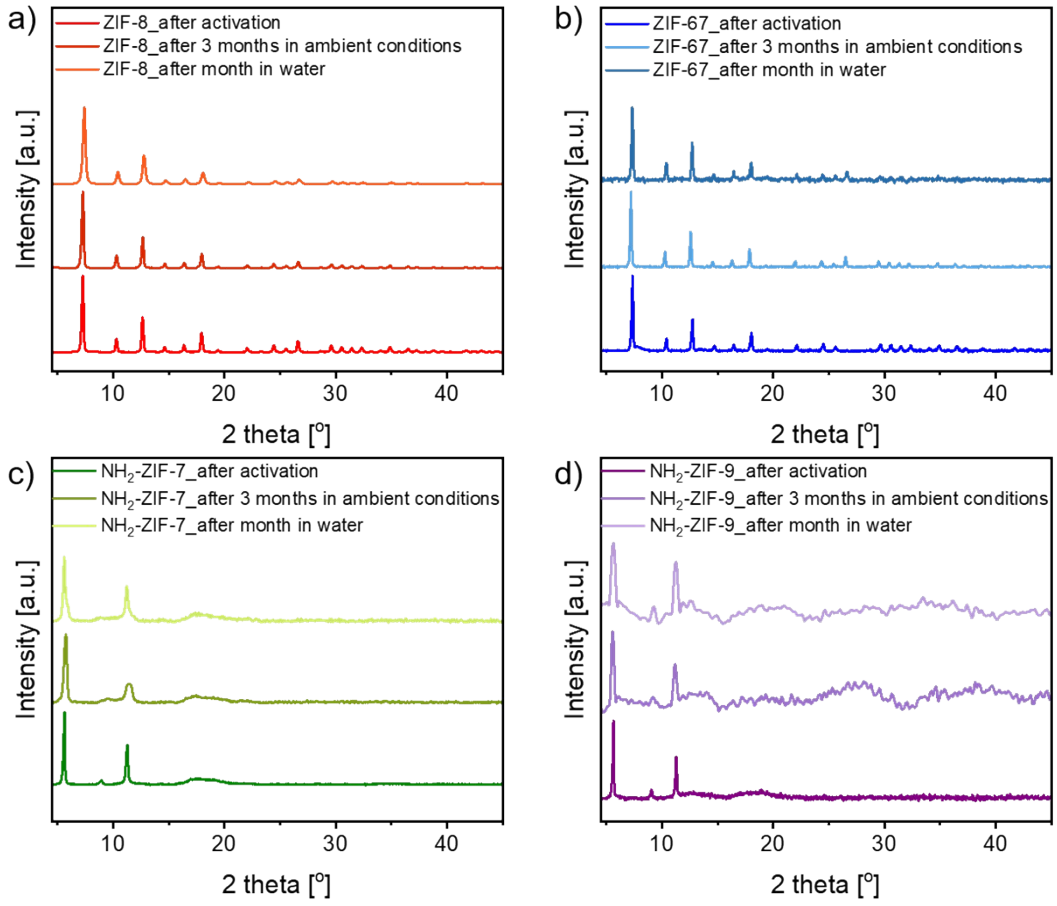

Figure S14. XRD of a) ZIF-8, b) ZIF-67, c) NH_2-ZIF-7 and d) NH_2-ZIF-9 after exposure to ambient conditions for three months and after immersion for one month in water (pH 5.5).

The stability of all compounds is first assessed by means of XRD analysis after exposure to ambient conditions for three months and after immersion for one month in water. All ZIFs exhibit excellent stability in ambient conditions, with no noticeable degradation observed over three months of storage under typical laboratory conditions (room temperature and normal humidity levels). Regarding stability in water (pH 5.5), all ZIFs show reasonable resistance to hydrolysis, maintaining their structural integrity for extended periods in slightly acid-aqueous environments. These findings demonstrate the robustness of these ZIFs under both ambient and aqueous conditions, making them suitable for a wide range of practical applications.

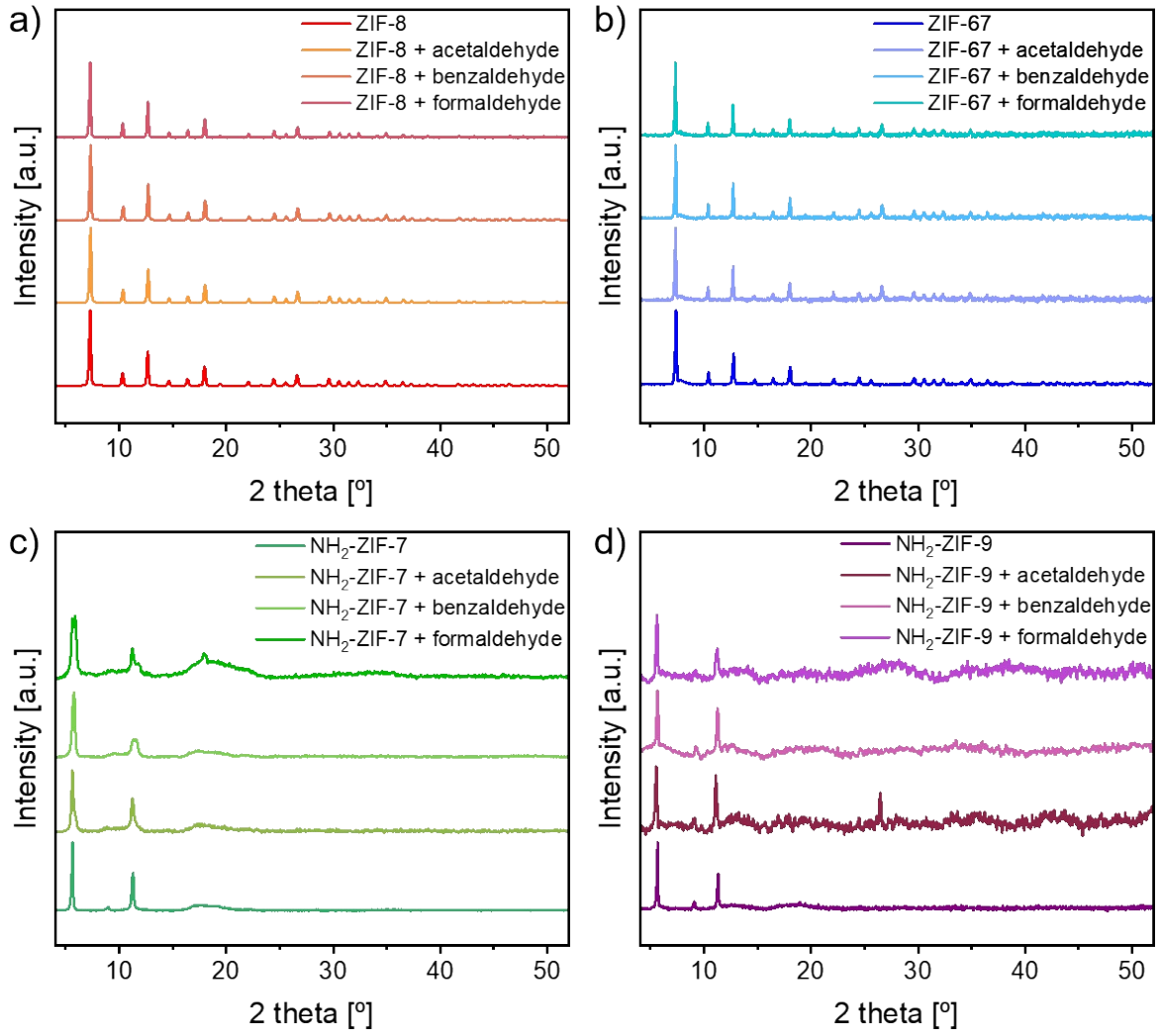

Figure S15. XRD of a) ZIF-8, b) ZIF-67, c) NH_2-ZIF-7 and d) NH_2-ZIF-9 upon exposure to aldehydes. Pristine ZIFs (black curves), and after exposure to acetaldehyde (red curves), benzaldehyde (blue curves), and formaldehyde (green curves).

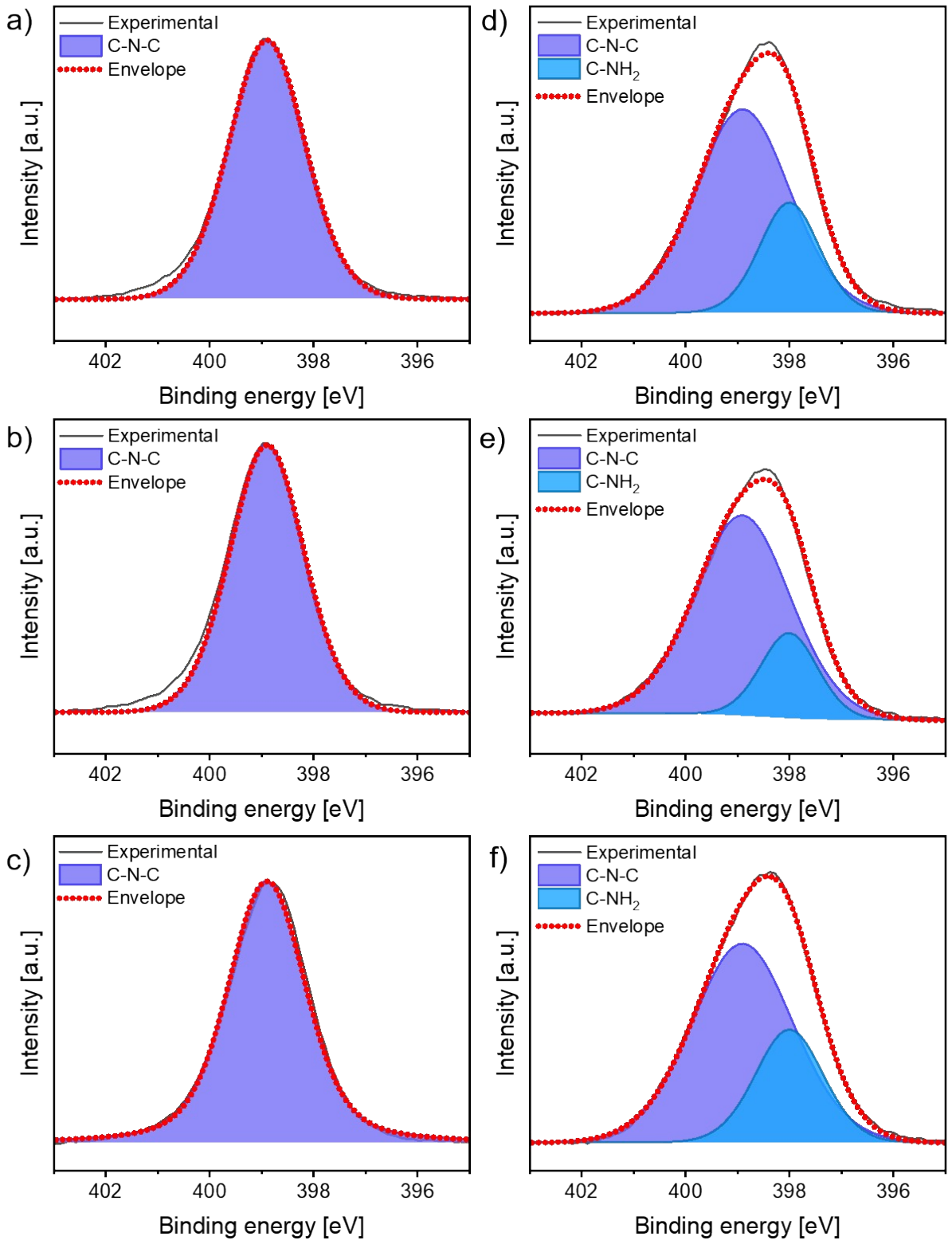

Figure S16. XPS, N1s spectra of (a-c) ZIF-8 and (d-f) NH_2-ZIF-7 upon exposure to a, d) acetaldehyde, b, e) benzaldehyde and c, f) formaldehyde.

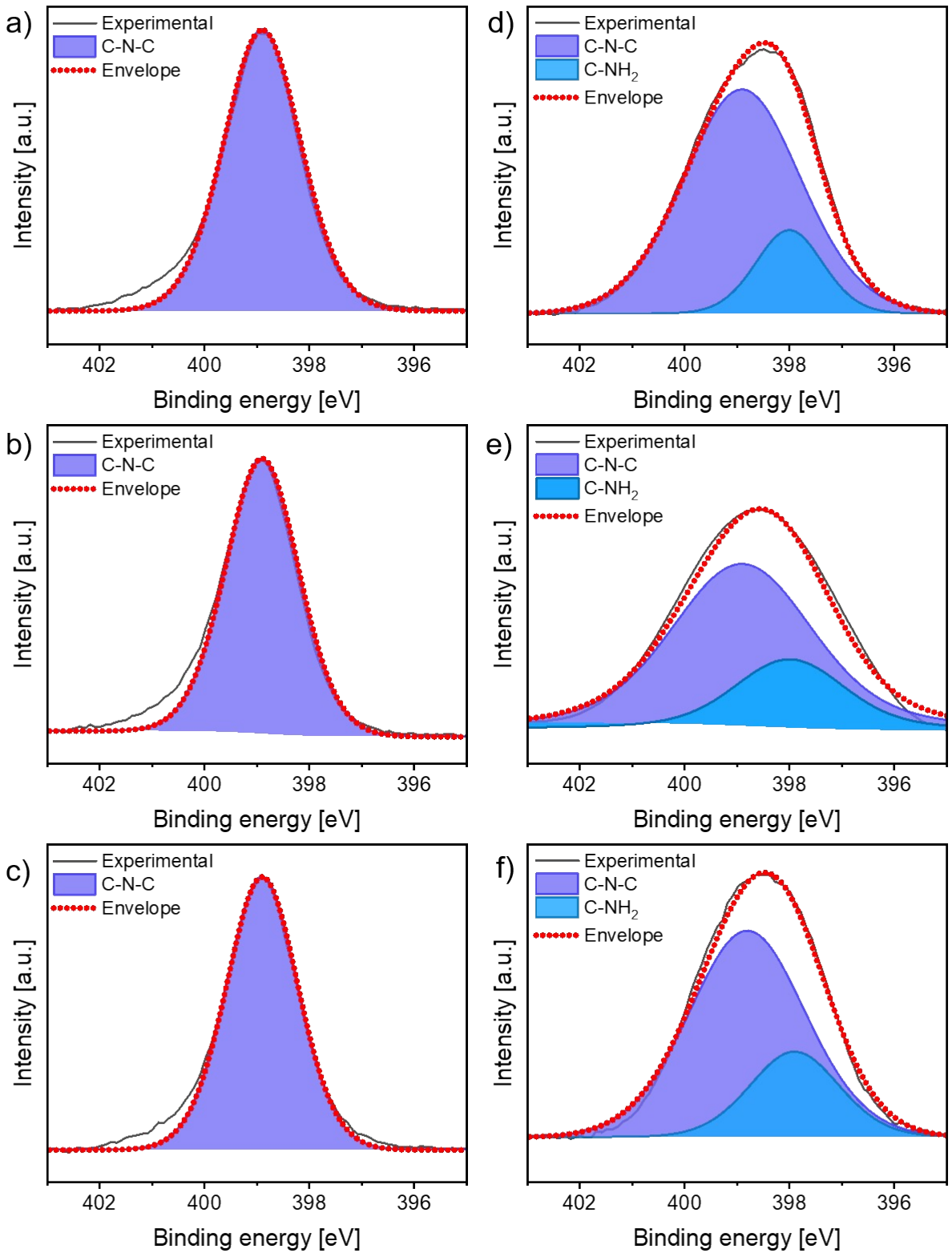

Figure S17. XPS, N1s spectra of (a-c) ZIF-67 and (d-f) NH_2-ZIF-9 upon exposure to a, d) acetaldehyde, b, e) benzaldehyde and c, f) formaldehyde.

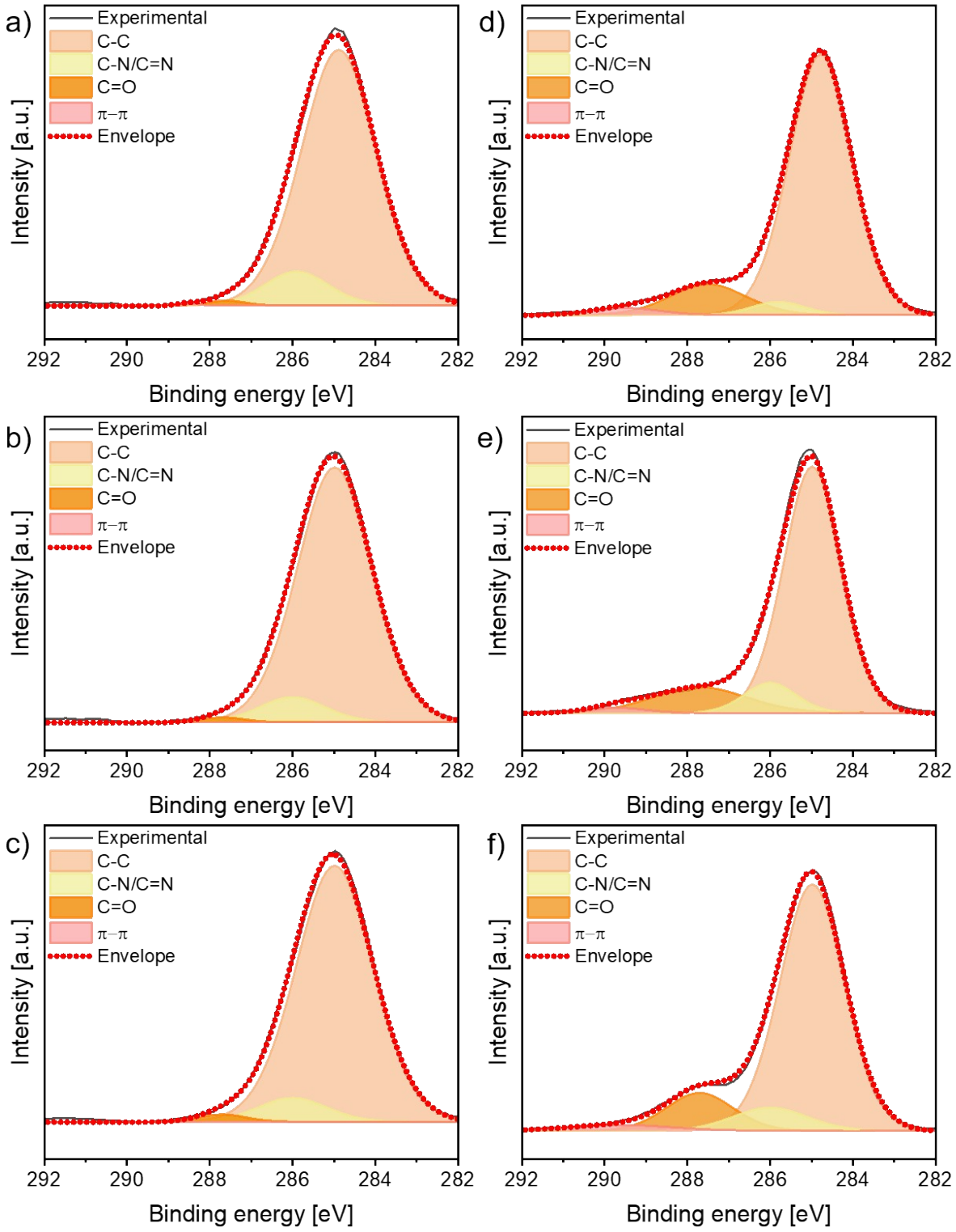

Figure S18. XPS, C1s spectra of (a-c) ZIF-8 and (d-f) NH_2-ZIF-7 upon exposure to a, d) acetaldehyde, b, e) benzaldehyde and c, f) formaldehyde.

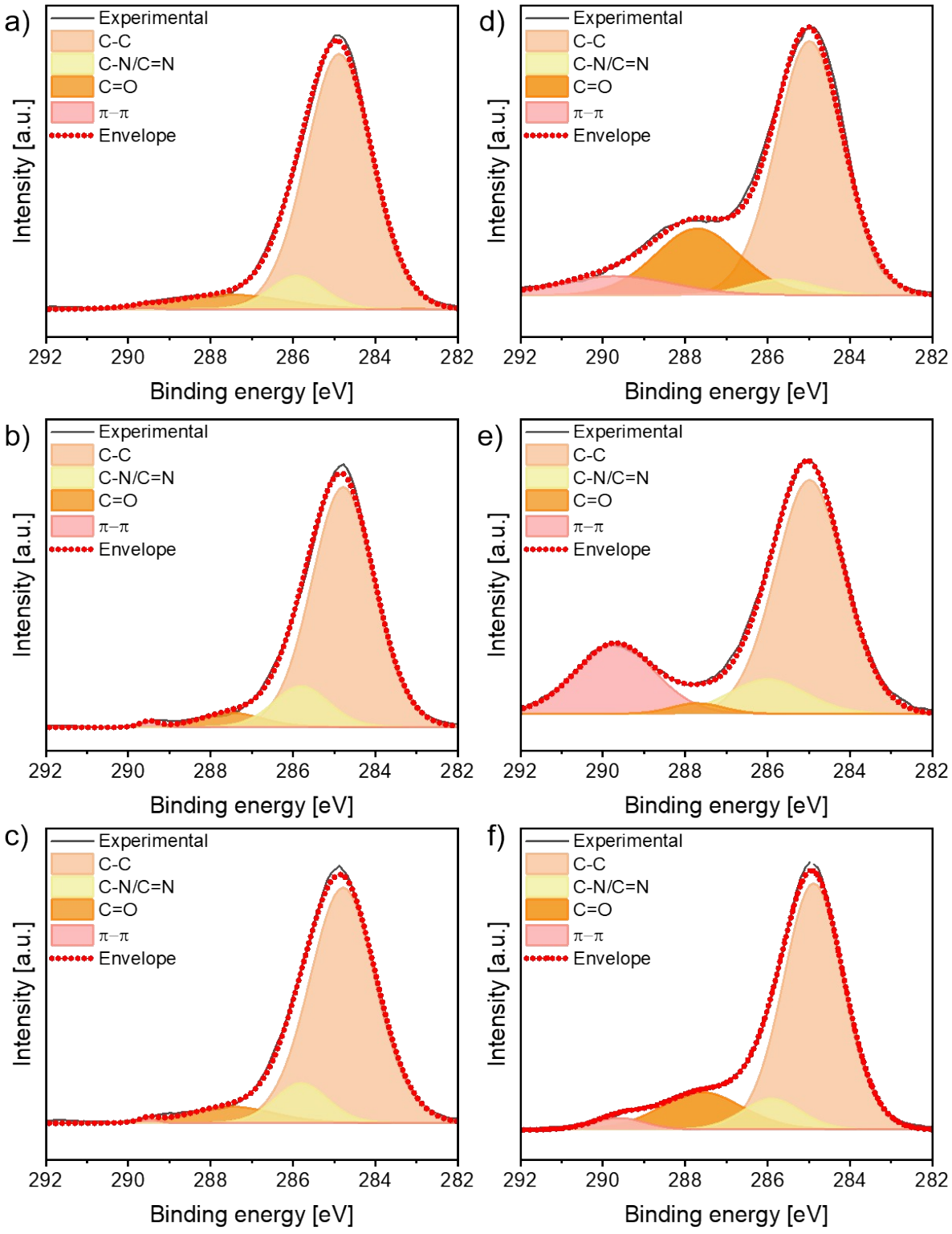

Figure S19. XPS, C1s spectra of (a-c) ZIF-67 and (d-f) NH_2-ZIF-9 upon exposure to a, d) acetaldehyde, b, e) benzaldehyde and c, f) formaldehyde.

Section D. Electrochemical sensing

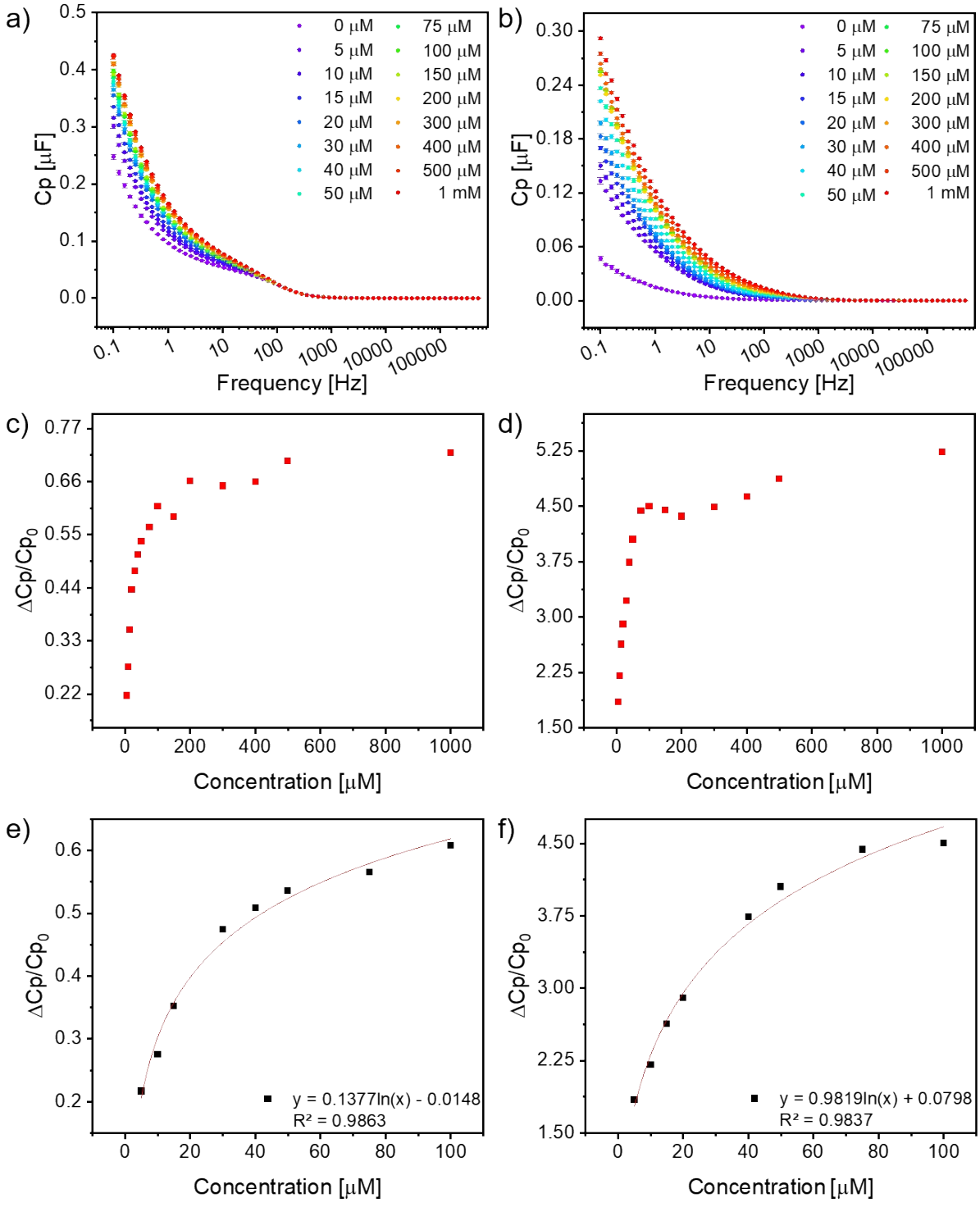

Figure S20. a-b) Capacitance response, c-d) normalized capacitance response ($\Delta Cp/Cp_0$) and e-f) logarithmic fitting in the calibration range of 5-100 μM of ZIF-8 as a function of the concentration of a, c, e) acetaldehyde, and b, d, f) benzaldehyde.

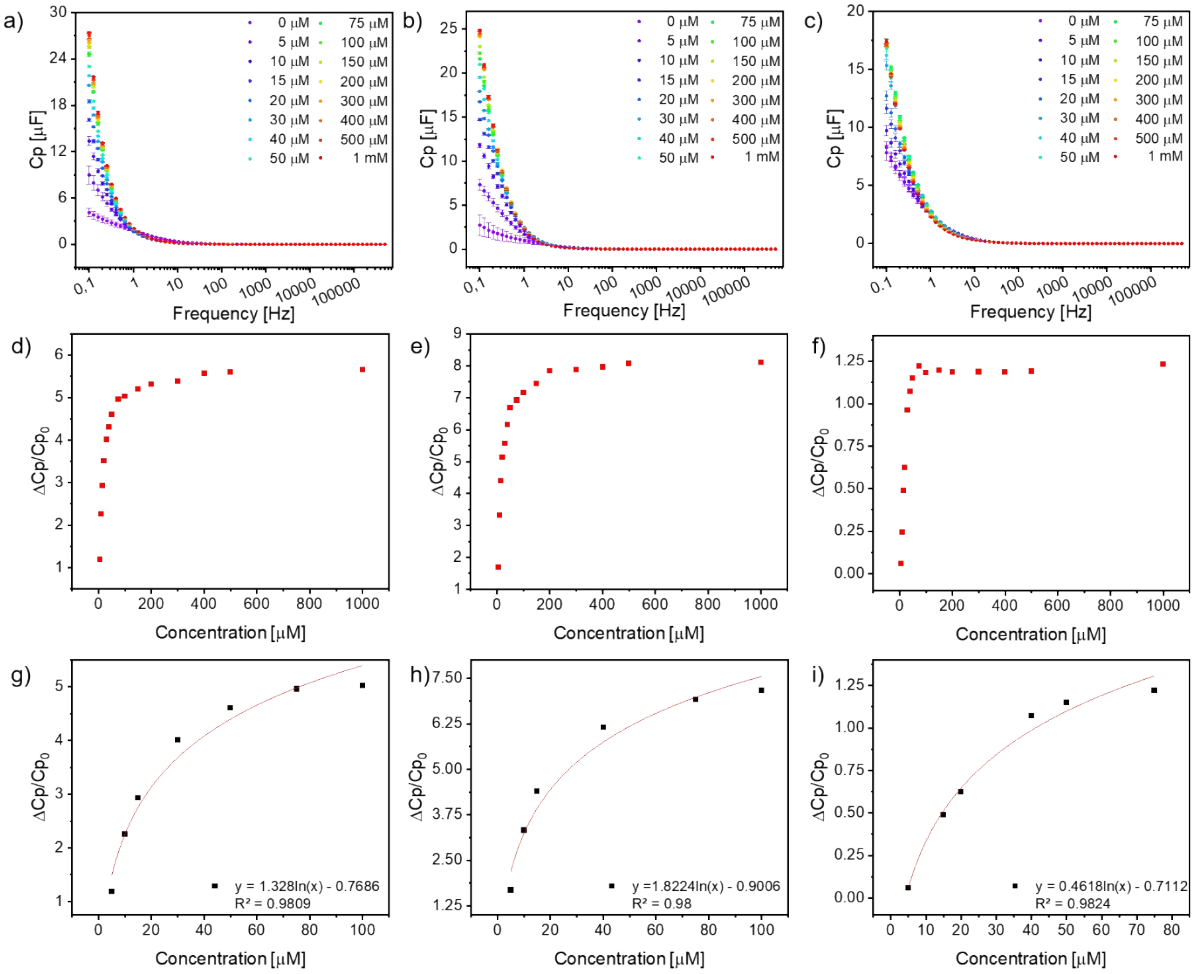

Figure S21. a-c) Capacitance response, d-f) normalized capacitance response ($\Delta Cp/Cp_0$) and g-i) logarithmic fitting in the calibration range of g, h) 5-100 µM and i) 5-75 µM of ZIF-67 as a function of the concentration of a, d, g) acetaldehyde, b, e, h) benzaldehyde and c, f, i) formaldehyde.

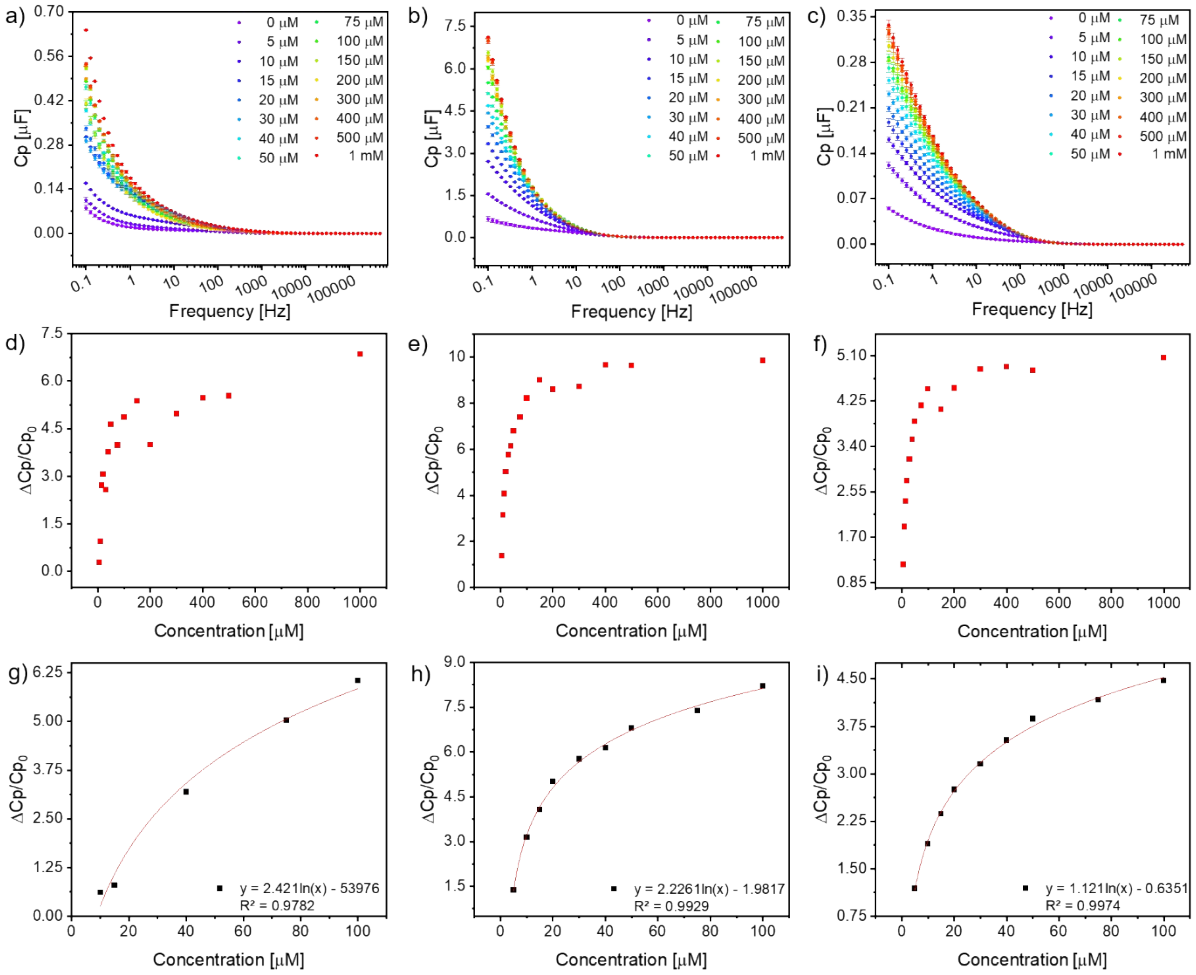

Figure S22. a-c) Capacitance response, d-f) normalized capacitance response ($\Delta Cp/Cp_0$) and g-i) logarithmic fitting in the calibration range of g) 10-100 μM and h, i) 5-100 μM of NH_2-ZIF-7 as a function of the concentration of a, d, g) acetaldehyde, b, e, h) benzaldehyde and c, f, i) formaldehyde.

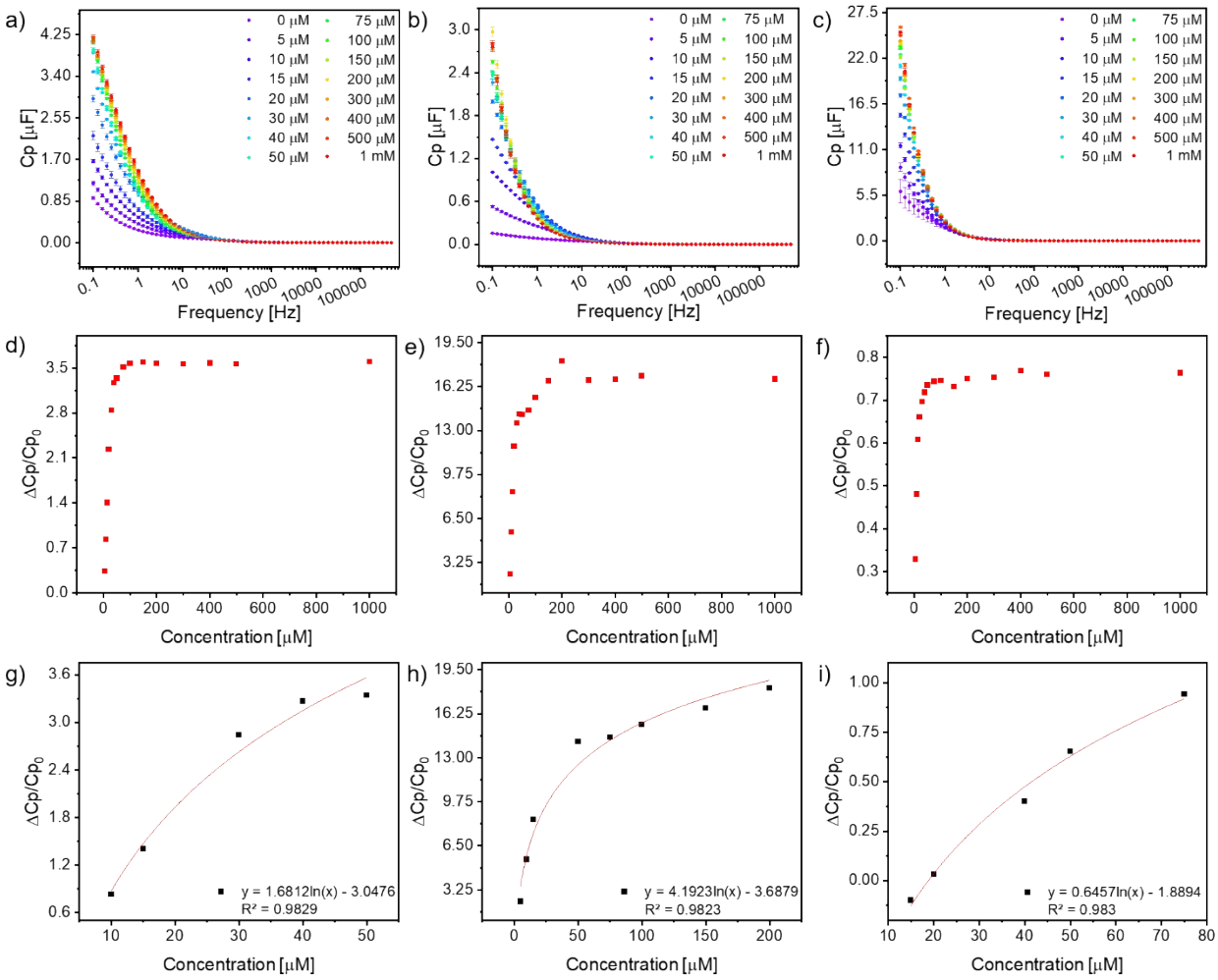

Figure S23. a-c) Capacitance response, d-f) normalized capacitance response ($\Delta Cp/Cp_0$) and g-i) logarithmic fitting in the calibration range of g) 10-50 μM, b) 5-200 μM and c) 15-75 μM of NH_2-ZIF-9 as a function of the concentration of a, d, g) acetaldehyde, b, e, h) benzaldehyde and c, f, i) formaldehyde.

Sensing mechanism

We can distinguish different detection mechanisms involved in monitoring aldehyde concentrations.

Effect of metal ion - Metal ions affect the geometry of the active center, and thus the size and shape of the pores, which in turn affects the availability of active sites for analytes. The metal used also affects the conductivity of the compound, and interactions between the active center and guest molecules can result in changes in conductivity.[13] As shown in Table S2, while the metal ion does not result in significant differences in surface area and porosity for ZIF-8 and ZIF-67, a notable effect is observed in NH_2-ZIF-7 and NH_2-ZIF-9. Specifically, using Co as the metal ion in NH_2-ZIF-9 produces a ZIF with a surface area and total pore volume that are 4 and 6 times higher, respectively, compared to its Zn-based counterpart (NH_2-ZIF-7). When the sensitivity towards formaldehyde, acetaldehyde and benzaldehyde of the ZIFs based on Zn and Co is compared (Fig. 3d) it can be seen that in most of the cases the sensitivity of Co-based ZIFs is higher. This is likely due to the enhanced conductivity provided by Co as the metal ion, which facilitates charge transfer during the sensing process. Additionally, the higher surface area and pore volume of NH_2-ZIF-9, increase the availability of active sites for analyte interaction. The larger pore volume also allows for better diffusion of aldehyde molecules, improving their accessibility to the active sites. Moreover, cobalt's electronic properties may enhance interactions between the active center and the aldehydes, potentially strengthening binding or catalytic activity. There are only two cases where the sensitivity was higher for Zn-based ZIFs. ZIF-8 demonstrated higher sensitivity towards formaldehyde than ZIF-67, likely due to its larger pore volume and higher affinity for smaller molecules like formaldehyde, which enhances its trapping efficiency. Similarly, NH_2-ZIF-7 exhibited higher sensitivity towards acetaldehyde than NH_2-ZIF-9. This could be attributed to differences in pore geometry and surface functionalization, where the Zn-based NH_2-ZIF-7 may provide a more favorable environment for interactions with acetaldehyde, possibly due to better alignment of the analyte with the imine bond formation mechanism.

Effect of amino groups and benzene ring – While the presence of a benzene ring in the ZIF structure reduces the specific surface area, it simultaneously introduces an additional interaction mechanism between the ZIF framework and aldehydes. This effect is particularly significant in the case of benzaldehyde, which also contains a benzene ring. XPS analysis after the reaction with aldehydes reveals the appearance of a band associated with π-π interactions, indicating the overlap of conjugated systems, i.e., benzene rings. The amino group provides another key interaction mechanism by enabling the formation of an imine bond between the amino group of the ZIF and the carbonyl group of the aldehyde. This imine bond formation has

been confirmed by XPS analysis before and after reactions of NH_2-ZIFs with aldehydes. Additionally, the amino group facilitates hydrogen bonding, as the hydrogen from the amino group interacts with the oxygen of the aldehyde's carbonyl group.[14]

It is worth noting that ZIFs based on 2-aminobenzimidazole have demonstrated significantly higher sensitivities towards all three aldehydes compared to their counterparts based on 2-methylimidazole. This enhanced sensitivity arises from the dual contributions of the amino group and the benzene ring. While 2-methylimidazole-based ZIFs primarily rely on hydrogen bonding, 2-aminobenzimidazole-based ZIFs incorporate both imine bond formation (applicable to all three aldehydes) and π-π interactions (specific to benzaldehyde). These combined mechanisms result in greater sensitivity to aldehydes overall. However, when comparing the sensitivity of benzene ring-based ZIFs (NH_2-ZIF-7 and NH_2-ZIF-9) toward different aldehydes, it becomes evident that sensitivity to benzaldehyde is not the highest in all cases. For NH_2-ZIF-7, the highest sensitivity is achieved with acetaldehyde, while for NH_2-ZIF-9, the highest sensitivity is observed for both formaldehyde and benzaldehyde. This suggests that while the presence of a benzene ring contributes to the overall sensitivity, it is not the sole determining factor for sensitivity to specific aldehydes. Instead, the interplay of multiple mechanisms—hydrogen bonding, imine bond formation, and π-π interactions—dictates the final sensitivity profile of these ZIFs.

Table S4. Key performance indicators of ZIF-8-based electrochemical sensors.

Aldehyde	Sensitivity [μM^{-1}]	LOD [μM]	Detection range [μM]	R^2
Acetaldehyde	0.1377	0.4991	5-100	0.9863
Benzaldehyde	0.9819	0.5379	5-100	0.9837
Formaldehyde	1.0712	0.5435	5-100	0.9806

Table S5. Key performance indicators of ZIF-67-based electrochemical sensors.

Aldehyde	Sensitivity [μM^{-1}]	LOD [μM]	Detection range [μM]	R^2
Acetaldehyde	1.3280	0.6398	5-100	0.9809
Benzaldehyde	1.8224	0.7251	5-100	0.9800
Formaldehyde	0.4618	0.6678	5-75	0.9824

Table S6. Key performance indicators of NH_2-ZIF-7-based electrochemical sensors.

Aldehyde	Sensitivity [μM^{-1}]	LOD [μM]	Detection range [μM]	R^2
Acetaldehyde	2.4210	0.9402	10-100	0.9782
Benzaldehyde	2.2261	0.5496	10-100	0.9875
Formaldehyde	1.1210	0.1974	5-100	0.9974

Table S7. Key performance indicators of NH_2-ZIF-9-based electrochemical sensors.

Aldehyde	Sensitivity [μM^{-1}]	LOD [μM]	Detection range [μM]	R^2
Acetaldehyde	1.6812	0.7441	10-50	0.9829
Benzaldehyde	4.1923	0.6464	5-200	0.9823
Formaldehyde	0.6457	0.8128	15-75	0.9830

Table S8. Aldehydes determination in tap water samples.

Sample	Aldehyde	Added amount [μM]	Found amount [μM]	Recovery [%]	RSD [%]
NH_2-ZIF-7	Benzaldehyde	10	9.62	96.22	9.04
NH_2-ZIF-7	Formaldehyde	10	9.52	95.25	1.9
		50	48.47	96.93	8.91
NH_2-ZIF-9	Acetaldehyde	10	9.59	95.87	9.04

State of the art

Table S9. State-of-the-art aldehyde sensors and their key performance indicators.

Material	Method	Analyte	Concentration range	LOD	R^2	Ref.
Tb@La-MOF	Fluorescence	Acetaldehyde	10–300 μM	5.5 μM	-	[15]
Eu^{3+}@ZUM	Fluorescence	Acetaldehyde	0 – 181.6012 μM	1.3166 μM	0.99094	[16]
Biofuel cells (BFCs)	Electrochemical	Acetaldehyde	5–200 μM	1 μM	0.998	[17]
ZIF-8	Electrochemical	Acetaldehyde	5-100 μM	0.4991 μM	0.9863	This work
ZIF-67	Electrochemical	Acetaldehyde	5-100 μM	0.6398 μM	0.9809	This work
NH_2-ZIF-7	Electrochemical	Acetaldehyde	10-100 μM	0.9402 μM	0.9782	This work
NH_2-ZIF-9	Electrochemical	Acetaldehyde	10-50 μM	0.7441 μM	0.9829	This work
Eu-MOF	Fluorescence	Benzaldehyde	0 to 1 mM	9.3 μM	0.9919	[18]
JXUST-19	Fluorescence	Benzaldehyde	0.01-0.08 mM	1.73 μM	0.999	[19]
Eu-MOF	Fluorescence	Benzaldehyde	0.2-20 μM	0.011 μM	0.998	[20]
JXUST-33	Fluorescence	Benzaldehyde	0-120 mM	0.4291 mM	0.95246	[21]
CdS-CNT NCs/GCE	Electrochemical	Benzaldehyde	0.1 nM to 1 mM	20.7312 μM	0.9992	[22]
CPE/Fe3O4/GO/PVP/ PANI/AOX	Electrochemical	Benzaldehyde	0.5–50 μM	0.4 μM	0.995	[23]
ZIF-8	Electrochemical	Benzaldehyde	5-100 μM	0.5379 μM	0.9837	This work

ZIF-67	Electrochemical	Benzaldehyde	5-100 μM	0.7251 μM	0.9800	This work
NH_2-ZIF-7	Electrochemical	Benzaldehyde	10-100 μM	0.5496 μM	0.9875	This work
NH_2-ZIF-9	Electrochemical	Benzaldehyde	5-200 μM	0.6464 μM	0.9823	This work
UiO-66-NH_2	Fluorescence	Formaldehyde	0.222–3.330 mM	0.1332 mM	0.9931	[24]
JNU-100	Fluorescence	Formaldehyde	0.74–12.34 μM	0.020 μM	0.9923	[25]
Al-MIL-53-N2H	Fluorescence	Formaldehyde	100–400 μM	8.37 μM	0.99	[26]
MIL-101(Cr)	Quartz crystal microbalance (QCM) nanosensor	Formaldehyde	0.0666 – 1.6649 mM	59.7383 uM	0.9988	[27]
SnO_2 nanosheets (calcinated Sn-based MOF)	Electrochemical	Formaldehyde	1.6649 – 99.8968 μM	1.0323 nM	0.986	[28]
ZnO@ZIF–8 Nanorods	Electrochemical	Formaldehyde	0.3330 – 6.6598 mM	0.1865 mM	0.9695	[29]
SPCPtEs	Electrochemical	Formaldehyde	60-460 μM	60 μM	0.0994	[30]
Pd NW arrays	Electrochemical	Formaldehyde	2 μM - 1 mM	0.5 μM	0.9982	[31]
Pd-modified TiO2 electrode	Electrochemical	Formaldehyde	0 - 17.7 mM	0.015 mM	0.996	[32]

AgPd/Ch–IL	Electrochemical	Formaldehyde	0.060 - 20 mM	0.022 mM	0.9988	[33]
PdSPE	Electrochemical	Formaldehyde	19.68 - 27.84 µM	2 µM	0.92	[34]
Screen-printed carbon electrodes modified with gold clusters	Electrochemical	Formaldehyde	1 - 10 mM	0.9 mM	0,9976	[35]
ZIF-8	Electrochemical	Formaldehyde	5-100 µM	0.5379 µM	0.9837	This work
ZIF-67	Electrochemical	Formaldehyde	5-100 µM	0.7251 µM	0.9800	This work
NH_2-ZIF-7	Electrochemical	Formaldehyde	10-100 µM	0.5496 µM	0.9875	This work
NH_2-ZIF-9	Electrochemical	Formaldehyde	5-200 µM	0.6464 µM	0.9823	This work

Aldehyde detection has been extensively studied using a variety of sensing technologies, with fluorescence-based sensors being one of the most commonly reported platforms due to their high sensitivity and rapid response. However, fluorescence sensors often face significant drawbacks, including complex instrumentation requirements, high costs, and susceptibility to environmental interference, which can limit their practicality for real-world applications. In contrast, electrochemical sensors are highly valued for their cost-effectiveness, simplicity, and ability to perform real-time, on-site analysis, making them a more feasible option for many practical scenarios. Despite this, challenges such as achieving high sensitivity, selectivity, and robustness remain prominent in existing electrochemical platforms. In this context, our study systematically investigates the use of ZIF-based frameworks, highlighting their potential as advanced electrochemical platforms for aldehyde sensing. Compared to the state-of-the-art, our ZIF-based sensors demonstrated competitive or superior performance in sensitivity and selectivity while maintaining robustness in complex real-world environments. For instance,

NH_2-ZIF-7 achieved a limit of detection (LOD) of 0.9402 μM for acetaldehyde, comparable to advanced biofuel cell sensors, and NH_2-ZIF-9 exhibited a broad detection range of 5–200 μM for formaldehyde, covering environmentally and biologically relevant concentrations. Furthermore, the use of NH_2-functionalized ZIFs leveraged imine bond formation to significantly enhance selectivity for aldehydes, distinguishing them from other systems that rely on less specific hydrogen bonding interactions. Additionally, our approach employs capacitance as a direct sensing parameter, avoiding the need for complex modeling or fitting, which simplifies the detection mechanism while ensuring reproducibility and practicality. These features position our ZIF-based sensors as a robust and versatile alternative to fluorescence-based systems, advancing the state-of-the-art in aldehyde sensing technologies.

References

1. A. Deacon, L. Briquet, M. Malankowska, F. Massingberd-Mundy, S. Rudić, T. I. Hyde, H. Cavaye, J. Coronas, S. Poulston and T. Johnson, *Commun Chem*, 2022, **5**, 18.
2. S. Gullace, V. Montes-García, V. Martín, D. Larios, V. Girelli Consolaro, F. Obelleiro, G. Calogero, S. Casalini and P. Samorì, *Small*, 2021, **17**, 2100755.
3. G. L.-C. K. Caamaño, R.Heras-Mozos, J. Glatz, P. Hernández-Muñoz, R. Gavara, M. Giménez-Marqués, *Dalton Trans.*, 2023, **52**, 17993-17999.
4. V. Montes-García, R. F. de Oliveira, Y. Wang, A. Berezin, P. Fanjul-Bolado, M. B. González García, T. M. Hermans, D. Bonifazi, S. Casalini and P. Samorì, *Advanced Functional Materials*, 2021, **31**, 2008554.
5. S. A. Moggach, T. D. Bennett and A. K. Cheetham, *Angewandte Chemie International Edition*, 2009, **48**, 7087-7089.
6. P. Zhao, G. I. Lampronti, G. O. Lloyd, M. T. Wharmby, S. Facq, A. K. Cheetham and S. A. T. Redfern, *Chemistry of Materials*, 2014, **26**, 1767-1769.
7. A. Schejn, L. Balan, V. Falk, L. Aranda, G. Medjahdi and R. Schneider, *CrystEngComm*, 2014, **16**, 4493-4500.
8. M. Afkhami-Ardekani, M. R. Naimi-Jamal, S. Doaee and S. Rostamnia, *Catalysts*, 2023, **13**, 9.
9. G. Zheng, Z. Chen, K. Sentosun, I. Pérez-Juste, S. Bals, L. M. Liz-Marzán, I. Pastoriza-Santos, J. Pérez-Juste and M. Hong, *Nanoscale*, 2017, **9**, 16645-16651.
10. L. Wang, Z. Wang, L. Xie, L. Zhu and X. Cao, *ACS Applied Materials & Interfaces*, 2019, **11**, 16619-16628.
11. Y. L. Xi Wang, *J. Mater. Chem. A*, 2016, **4**, 5247-5257.
12. X. Y. Chen, V.-T. Hoang, D. Rodrigue and S. Kaliaguine, *RSC Advances*, 2013, **3**, 24266-24279.
13. V. Rubio-Giménez, N. Almora-Barrios, G. Escorcia-Ariza, M. Galbiati, M. Sessolo, S. Tatay and C. Martí-Gastaldo, *Angewandte Chemie International Edition*, 2018, **57**, 15086-15090.
14. S. Bej, S. Mandal, A. Mondal, T. K. Pal and P. Banerjee, *ACS Applied Materials & Interfaces*, 2021, **13**, 25153-25163.
15. X. Liu, W. Tian, H. Liu, Y. Ma, D. Huo and C. Hou, *Spectrochimica Acta Part A: Molecular and Biomolecular Spectroscopy*, 2024, **322**, 124797.
16. X.-Y. Xu and B. Yan, *Journal of Materials Chemistry A*, 2017, **5**, 2215-2223.
17. L. Zhang, M. Zhou and S. Dong, *Analytical Chemistry*, 2012, **84**, 10345-10349.
18. X. Wang and W. Liu, *Dalton Transactions*, 2024, **53**, 11850-11857.
19. K. Wang, T.-F. Zheng, J.-L. Chen, H.-R. Wen, S.-J. Liu and T.-L. Hu, *Inorganic Chemistry*, 2022, **61**, 16177-16184.

20. N. Wu, H. Guo, X. Wang, L. Sun, T. Zhang, L. Peng and W. Yang, *Colloids and Surfaces A: Physicochemical and Engineering Aspects*, 2021, **616**, 126093.
21. R.-J. Zhang, J.-J. Wang, H. Xu, Z.-H. Zhu, T.-F. Zheng, Y. Peng, J.-L. Chen, S.-J. Liu and H.-R. Wen, *Crystal Growth & Design*, 2023, **23**, 5564-5570.
22. M. M. Rahman, *Materials Chemistry and Physics*, 2020, **245**, 122788.
23. S. Sadeghi, E. Fooladi and M. Malekaneh, *Electroanalysis*, 2015, **27**, 242-252.
24. K. Vellingiri, A. Deep, K.-H. Kim, D. W. Boukhvalov, P. Kumar and Q. Yao, *Sensors and Actuators B: Chemical*, 2017, **241**, 938-948.
25. Y.-B. Wei, M.-J. Wang, D. Luo, Y.-L. Huang, M. Xie, W. Lu, X. Shu and D. Li, *Materials Chemistry Frontiers*, 2021, **5**, 2416-2424.
26. S. Nandi, E. Sharma, V. Trivedi and S. Biswas, *Inorganic Chemistry*, 2018, **57**, 15149-15157.
27. E. Haghighi and S. Zeinali, *Microporous and Mesoporous Materials*, 2020, **300**, 110065.
28. X. Zhu, X. Zhang, X. Chang, J. Li, L. Pan, Y. Jiang, W. Gao, C. Gao and S. Sun, *Sensors and Actuators B: Chemical*, 2021, **347**, 130599.
29. H. Tian, H. Fan, M. Li and L. Ma, *ACS Sensors*, 2016, **1**, 243-250.
30. L. del Torno-de Román, M. A. Alonso-Lomillo, O. Domínguez-Renedo, C. Merino-Sánchez, M. P. Merino-Amayuelas and M. J. Arcos-Martínez, *Talanta*, 2011, **86**, 324-328.
31. Y. Zhang, M. Zhang, Z. Cai, M. Chen and F. Cheng, *Electrochimica Acta*, 2012, **68**, 172-177.
32. Q. Yi, F. Niu and W. Yu, *Thin Solid Films*, 2011, **519**, 3155-3161.
33. Q. Wang, J. Zheng and H. Zhang, *Journal of Electroanalytical Chemistry*, 2012, **674**, 1-6.
34. J. P. Metters, F. Tan and C. E. Banks, *Journal of Solid State Electrochemistry*, 2013, **17**, 1553-1562.
35. M. R. Baez-Gaxiola, C. Fernández-Sánchez and E. Mendoza, *Analytical Methods*, 2015, **7**, 538-542.